

Optics of Solar Concentrators. Part III: Models of Light Collection of 3D-CPCs under Direct and Lambertian Irradiation

Antonio Parretta^{1,2,*}, Erica Cavallari²

¹ENEA C.R. "E. Clementel", Via Martiri di Monte Sole 4, Bologna (BO), Italy

²Physics Department, University of Ferrara, Via Saragat 1, Ferrara (FE), Italy

Abstract The optical properties of nonimaging solar concentrators irradiated in direct mode by diffused Lambertian beams are investigated in detail adopting original simulation methods. These methods were not limited to investigate useful properties for the practical application of the concentrators, but were also used to study them as optical elements with specific transmission, reflection and absorption characteristics. We have investigated, therefore, besides the flux transmitted to the receiver, also the flux back reflected from input aperture and that absorbed on the wall of the concentrator. We have simulated the transmission, reflection and absorption efficiencies, the average number of reflections of the transmitted or reflected rays, their angular divergence and the distribution of flux on the receiver and on the internal wall surface, as function of the angular divergence of the input beam and of the reflectivity of the internal wall. The presented simulation methods can be fruitfully applied to any other type of solar concentrator.

Keywords Solar concentrator, Light collection, Optical simulation, Optical modeling, Nonimaging optics

1. Introduction

A review of the theoretical models of light irradiation and collection in solar concentrators (SC) was presented in the first part of this work [1]. In the second part [2] we presented the optical simulations of those models applied to nonimaging SC irradiated by direct and collimated beams. The importance of this irradiation lies in the fact that it represents the typical operating condition of a SC. We have chosen, for the optical simulations, a class of nonimaging SC of the type 3D-CPC (Three-Dimensional Compound Parabolic Concentrators) [3-9] to be used mainly as primary elements of a concentrator system. In this paper we extend the study of these SC by investigating diffused irradiation conditions, which are well represented by lambertian beams (beams with constant radiance) with variable angular aperture. The results of our work can be extended in this way to CPC used as secondary elements of concentration.

Our interest on these SC is that they allow to reach very high concentration levels, comparable to the theoretical ones, and that their optical transmission efficiency is quite constant within a defined angle of incidence of the input beam. A further advantage of these SC is that they operate

with reflective surfaces that do not induce spectral dispersion of light.

We have simulated the optical behavior of the nonimaging SC by investigating its transmission, reflection and absorption properties, and we have defined new optical quantities. In particular, we have examined: i) the transmitted flux in terms of the optical transmission efficiency, average number of internal reflections of the transmitted rays, spatial distribution of the flux density on the receiver, angular distribution of radiance at the exit aperture; ii) the flux reflected from the input aperture in terms of reflection efficiency, angular divergence and average number of reflections; iii) the absorbed flux in terms of absorption efficiency and distribution of the absorbed flux on the internal wall of the CPC. In this way, all the optical features of the SC, considered as a generic optical element interacting with a lambertian beam, were analyzed. The methods of simulation and elaboration of the optical data presented in this work can be considered as general tools for the analysis of any other optical device.

2. The Compound Parabolic Concentrator (CPC)

The Compound Parabolic Concentrator (CPC) is a nonimaging concentrator developed by R. Winston [3] to efficiently collect Cherenkov radiation in high energy experiments. Since then, the nonimaging concentrators have

* Corresponding author:

parretta@fe.infn.it (Antonio Parretta)

Published online at <http://journal.sapub.org/optics>

Copyright © 2015 Scientific & Academic Publishing. All Rights Reserved

been widely used to concentrate sunlight [4-18]. The CPC is a reflective concentrator with a profile obtained by the combination of two parabolas, and is characterized by a step-like transmission efficiency allowing the efficient collection of light from 0° to a maximum angle, the acceptance angle θ_{acc}^{coll} , where the suffix “coll” means that the irradiation is done with a collimated beam.

Fig. 1 shows the 3D-CPC used in this work for the optical simulations. It is the same that was used in the previous paper of this series [2]. It is characterized by a maximum divergence of rays at exit aperture equal to 90° , and then only two independent parameters are required for defining its shape.

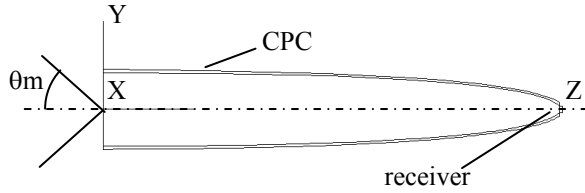


Figure 1. Longitudinal section of the Compound Parabolic Concentrator (CPC) used in this work for the optical simulations. The angle $\sin^2 \theta_m$ is the maximum angle of aperture of the input Lambertian beam. The angle of acceptance of a parallel beam is $\theta_{acc}^{coll} = 5^\circ$

We have chosen the acceptance angle at parallel beam, $\theta_{acc}^{coll} = 5^\circ$, and the length $L = 150$ mm. The focal length of the parabolic profile, $f = 1.14$ mm, the radius of input aperture, $a = 12.035$ mm, and the radius of output aperture, $a' = 1.052$ mm, become [2]:

$$f = a'(1 + \sin \theta_{acc}^{coll}) \quad (1)$$

$$a' = a \cdot \sin \theta_{acc}^{coll} \quad (2)$$

$$L = (a + a') \cdot \text{ctg} \theta_{acc}^{coll} \quad (3)$$

Even if not so interesting for practical use (it is too long respect to its input diameter), nevertheless the chosen canonical CPC is useful to be studied as representative of ideal nonimaging concentrators characterized by a maximum exit angle of 90° . In addition, the characterization methods here described can be usefully applied to any other concentrator, ideal or not. The only change made to the concentrator during the optical simulations was that of reflectivity of the internal wall, R_w ; all the other added devices (absorbers, screens, etc.) were external to the concentrator and were used only as tools to improve the knowledge of its optical properties. For the reflectivity of the internal wall we have used only high values ($0.8 \div 1.0$); when not specified, it is equal to 1 (no optical loss inside the concentrator). All the optical simulations were carried out by using the TracePro ray-tracing software of Lambda Research [19].

The flux at input of the CPC is a Lambertian flux

characterized by a constant radiance L_{in} and by a variable angular aperture θ_m . The total flux at input is then a function of θ_m and is expressed by [1]:

$$\Phi_{in}(\theta_m) = L_{in} \cdot A_{in} \cdot 2\pi \cdot \int_0^{\theta_m} d\theta_{in} \cdot \sin \theta_{in} \cdot \cos \theta_{in} = \dots \quad (4)$$

$$\dots = \pi \cdot L_{in} \cdot A_{in} \cdot \sin^2 \theta_m$$

where θ_{in} is the incident polar angle. In order to keep constant the radiance at input of the CPC, we have used in the simulations a number of input rays, that is an input flux, proportional to $\sin^2 \theta_m$.

3. Analysis of the Transmitted Flux

3.1. Analysis of the Total Flux Transmitted to Receiver

To study the flux transmitted to the exit aperture of the CPC, we have closed the exit aperture by an ideal absorber, so all the rays reaching the aperture can be counted and analyzed by the simulation program [19]. The flux transmitted to the exit aperture is given by:

$$\Phi_{\tau}(\theta_m) = 2\pi \cdot L_{in} \cdot A_{in} \cdot \int_0^{\theta_m} d\theta_{in} \cdot \sin \theta_{in} \cdot \cos \theta_{in} \cdot \eta_{dir}^{coll}(\theta_{in}) \quad (5)$$

where $\eta_{dir}^{coll}(\theta_{in})$ is the transmission efficiency of the CPC under direct and collimated irradiation, and is a function of the incident polar angle θ_{in} [1, 2] (see Fig.2).

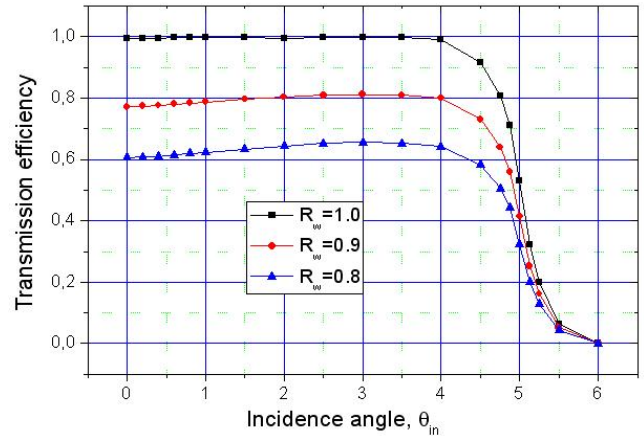


Figure 2. Optical transmission efficiency $\eta_{dir}^{coll}(R_w, \theta_{in})$ of the 3D-CPC calculated for three wall reflectivities: $R_w = 1.0, 0.9$ and 0.8

The input lambertian flux was simulated by sending to the input aperture a number of rays, each with a constant flux of 1W, following the $\sin^2 \theta_m$ rule (see Eq. (4)), corresponding, in this simulation, to 50k rays at $\theta_m = 10^\circ$.

Fig. 3 shows the number of the incident, transmitted and reflected rays vs. θ_m , measured for a unitary wall reflectivity. In this case we have no optical loss on the wall of the CPC, but only loss due to the back reflected rays. We can see that, as long as $\theta_m < \theta_{acc}^{coll}$, due to the square shape of the transmission efficiency of the CPC (see Fig. 2), all the input rays are transmitted, whereas, at $\theta_m \approx \theta_{acc}$, the transmitted rays stop growing and the reflected rays begin to appear and grow following the growth of the incident rays.

As well as we have defined a transmission efficiency for a parallel beam at input of concentrator (see Fig. 2), we define the transmission efficiency for a lambertian beam at input of concentrator, and call it “direct lambertian transmittance”, τ_{dir}^{lamb} [1].

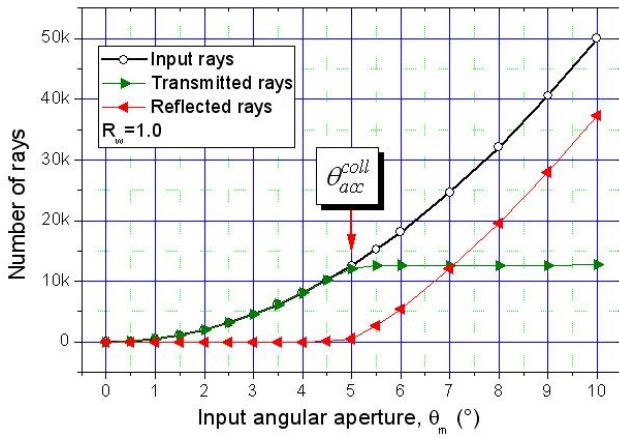


Figure 3. Number of incident, transmitted and reflected rays vs. the angular aperture of the Lambertian beam θ_m , calculated for a unitary wall reflectivity

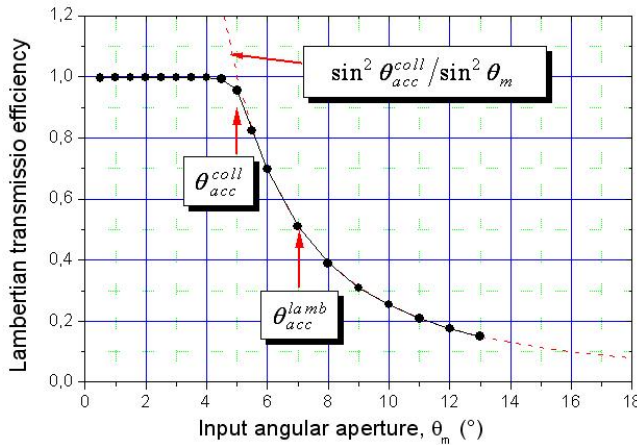


Figure 4. Lambertian transmission efficiency of the CPC calculated as function of the angular aperture of the Lambertian beam, θ_m , for a unitary wall reflectivity

This quantity refers to an angular aperture of the Lambertian beam equal to 90° . If the lambertian beam at input is limited by the angular aperture θ_m , the above

quantity becomes $\tau_{dir}^{lamb}(\theta_m)$. We have added the term “dir” to distinguish the Lambertian beam that we send to the entrance aperture of the concentrator, from the Lambertian beam that we send to the exit aperture of the concentrator, and that we will indicate by the term “inv”. The properties of a CPC concentrator irradiated by an “inverse” Lambertian beam will be discussed in a future paper of this series. The Lambertian transmission efficiency of the CPC is expressed [1] by the ratio between output and input flux:

$$\begin{aligned} \tau_{dir}^{lamb}(\theta_m) &= \frac{\Phi_\tau(\theta_m)}{\Phi_{in}(\theta_m)} = \dots \\ &= \frac{2}{\sin^2 \theta_m} \cdot \int_0^{\theta_m} d\theta_{in} \cdot \sin \theta_{in} \cdot \cos \theta_{in} \cdot \eta_{dir}^{coll}(\theta_{in}) \end{aligned} \quad (6)$$

The plot of $\tau_{dir}^{lamb}(\theta_m)$, simulated for a unitary wall reflectivity, is shown in Fig. 4. It is interesting to compare the behavior of $\tau_{dir}^{lamb}(\theta_m)$ with that of $\eta_{dir}^{coll}(\theta_{in})$ (see Fig.2). We obtain a step-like transmission efficiency curve also for a Lambertian beam irradiation, with the efficiency almost constant until about the acceptance angle ($\theta_{acc}^{coll} = 5^\circ$), but, differently from the transmission efficiency curve $\eta_{dir}^{coll}(\theta_{in})$, now the $\tau_{dir}^{lamb}(\theta_m)$ curve decreases slowly at increasing θ_m . The reason is that, for $\theta_m > \theta_{acc}^{coll}$, a constant portion of the input beam is always collected, and the Lambertian transmission efficiency at these conditions can be expressed by (on the assumption that $R_w = 1.0$):

$$\begin{aligned} \tau_{dir}^{lamb}(\theta_m > \theta_{acc}^{coll}) &= \dots \\ &= \frac{2}{\sin^2 \theta_m} \cdot \int_0^{\theta_m} d\theta_{in} \cdot \sin \theta_{in} \cdot \cos \theta_{in} \cdot \eta_{dir}^{coll}(\theta_{in}) \approx \dots \\ &\approx \frac{2}{\sin^2 \theta_m} \cdot \int_0^{\theta_{acc}^{coll}} d\theta_{in} \cdot \sin \theta_{in} \cdot \cos \theta_{in} \cdot \eta_{dir}^{coll}(\theta_{in}) \approx \dots \\ &\approx \frac{\sin^2 \theta_{acc}^{coll}}{\sin^2 \theta_m} \cdot \bar{\eta}_{dir}^{coll}(\theta_{in}) \approx \frac{\sin^2 \theta_{acc}^{coll}}{\sin^2 \theta_m} \end{aligned} \quad (7)$$

In Eq. (7) we have put $\bar{\eta}_{dir}^{coll}(\theta_{in}) \approx 1$, as it can be seen from the curve of Fig. 2 corresponding to $R_w = 1.0$. Fig. 4 shows the Lambertian transmission efficiency of the CPC compared to the $\sin^2 \theta_{acc}^{coll} / \sin^2 \theta_m$ function. The perfect correspondence between the two curves when $\theta_m > \theta_{acc}^{coll}$ is clearly evident.

Now we are able to define a new optical quantity, the angular aperture of the input Lambertian beam corresponding to the halving of the direct Lambertian transmittance at $\theta_m = 0^\circ$. We call this angle the

“Lambertian acceptance angle”, θ_{acc}^{lamb} , indicated in Fig. 4 together with θ_{acc}^{coll} , the acceptance angle at parallel beam irradiation. The quantity θ_{acc}^{lamb} is immediately derived from Eq. (7), and is about 7.1° for our CPC with $\theta_{acc}^{coll} = 5.0^\circ$:

$$\theta_{acc}^{lamb} = \sin^{-1}[\sqrt{2} \cdot \sin \theta_{acc}^{coll}] = \sin^{-1}[\sqrt{2} \cdot \sin 5^\circ] = 7.08^\circ \quad (8)$$

Contrary to the “parallel” transmission efficiency (Fig. 2), the Lambertian transmission efficiency never reaches the zero because there is always a portion of lambertian beam that is transmitted; in fact, it decreases reaching a minimum at $\theta_m = 90^\circ$ equal to $\sin^2 \theta_{acc}^{coll}$ ($\approx 7.6 \cdot 10^{-3}$ for $\theta_{acc}^{coll} = 5^\circ$).

Until now we have not yet analyzed the effect of R_w on the studied quantities. We do it starting with the direct Lambertian transmittance, calculated for three wall reflectivities: $R_w = 1.0, 0.9$ and 0.8 (see Fig. 5).

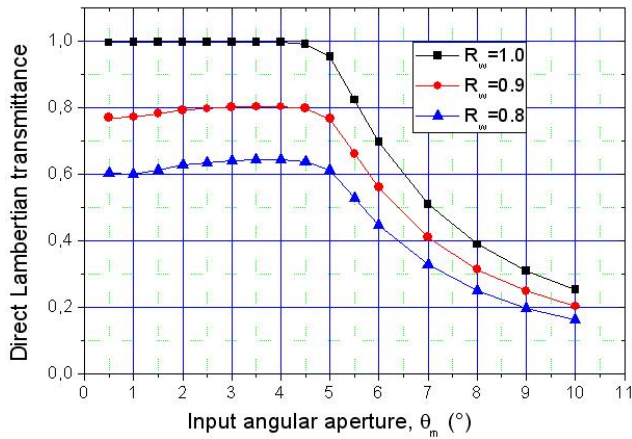


Figure 5. The Lambertian transmission efficiency calculated for three different wall reflectivities: $R_w = 1.0, 0.9$ and 0.8

3.2. Average Number of Reflections of the Total Absorbed Rays

The analysis of the three curves of $\tau_{dir}^{lamb}(R_w, \theta_m)$ allows deriving the average number of reflections experienced by the transmitted rays. In this regard we will make use of a formula similar to Eq. (24) used in [2], replacing $\eta_\tau(R_w, \theta_{in}) = \eta_{dir}^{coll}(R_w, \theta_{in})$ with $\tau_{dir}^{lamb}(R_w, \theta_m)$:

$$\bar{N}_\tau(R'_w, R''_w, \theta_m) = \frac{\log \left[\frac{\tau_{dir}^{lamb}(R'_w, \theta_m) \cdot N_\tau(R''_w, \theta_m)}{\tau_{dir}^{lamb}(R''_w, \theta_m) \cdot N_\tau(R'_w, \theta_m)} \right]}{\log \left[\frac{R'_w}{R''_w} \right]} \quad (9)$$

where $N_\tau(R_w, \theta_m)$ represents the number of transmitted rays. The average number of reflections has been calculated by using three pairs of wall reflectivities: (1.0-0.9); (1.0-0.8); (0.9-0.8).

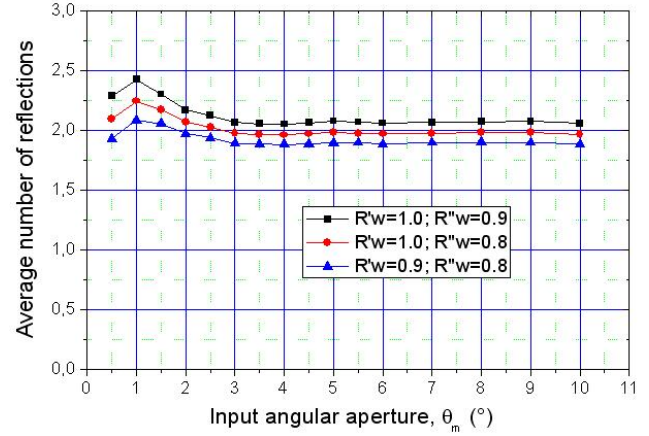


Figure 6. Average number of reflections experienced by the transmitted rays, as function of the angular aperture of the Lambertian beam, calculated for three pairs of wall reflectivities: (1.0-0.9); (1.0-0.8); (0.9-0.8)

The results are reported in Fig. 6 and show that the average number of reflections of the transmitted rays is practically independent on the angular aperture of the Lambertian beam and equal to ≈ 2 . This result is in good agreement with what was found [2] by analyzing the average number of reflections of the transmitted beam when the CPC is irradiated with a parallel beam at different polar angles respect to the optical axis.

3.3. Lambertian Concentration Ratio

We now introduce the quantity “direct Lambertian concentration ratio”, C_{dir}^{lamb} , defined in [1] as the ratio between the average output, or transmitted, radiance and the constant input radiance. When the lambertian beam at input has an angular aperture θ_m , the direct Lambertian concentration ratio is indicated as $C_{dir}^{lamb}(\theta_m)$.

We start calculating the average output radiance:

$$\begin{aligned} \bar{L}_\tau(\theta_m) &= \frac{\Phi_\tau(\theta_m)}{\pi \cdot A_{out}} = \dots \\ &= 2 \cdot L_{in} \cdot C_{geo} \cdot \int_0^{\theta_m} d\theta_{in} \cdot \sin \theta_{in} \cdot \cos \theta_{in} \cdot \eta_{dir}^{coll}(\theta_{in}) \end{aligned} \quad (10)$$

and the direct lambertian concentration ratio becomes:

$$\begin{aligned} C_{dir}^{lamb}(\theta_m) &= \frac{\bar{L}_\tau(\theta_m)}{L_{in}} = \dots \\ &= 2 \cdot C_{geo} \cdot \int_0^{\theta_m} d\theta_{in} \cdot \sin \theta_{in} \cdot \cos \theta_{in} \cdot \eta_{dir}^{coll}(\theta_{in}) = \dots \\ &= \frac{\Phi_\tau(\theta_m)}{\Phi_{in}(\theta_m)} \cdot C_{geo} \cdot \sin^2 \theta_m = \tau_{dir}^{lamb}(\theta_m) \cdot C_{geo} \cdot \sin^2 \theta_m \end{aligned} \quad (11)$$

Fig. 7 shows $\bar{L}_\tau(\theta_m)$, expressed in (W/mm²·sr) and calculated for three wall reflectivities: $R_w=1.0, 0.9$ and 0.8 .

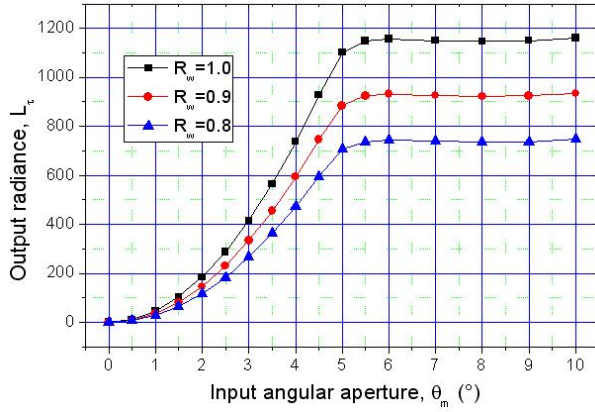


Figure 7. Average output radiance $\bar{L}_\tau(\theta_m)$ of the transmitted flux, calculated for three wall reflectivities: 1.0, 0.9 and 0.8

The direct Lambertian concentration ratio $C_{dir}^{lamb}(\theta_m)$ calculated from Eq. (11) is reported in Fig. 8.

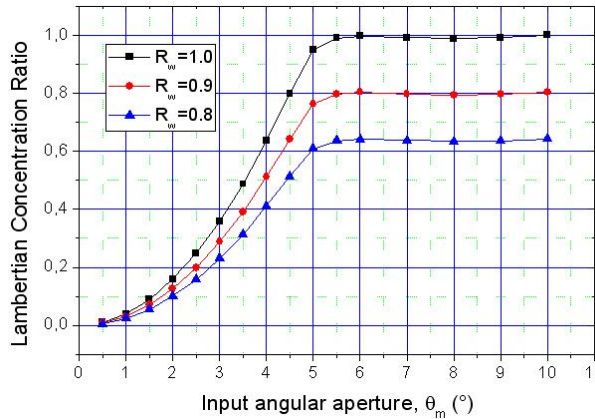


Figure 8. Direct lambertian concentration ratio, $C_{dir}^{lamb}(\theta_m)$ calculated for three wall reflectivities: $R_w = 1.0, 0.9$ and 0.8

Fig. 8 shows that $C_{dir}^{lamb}(\theta_m)$ is always ≤ 1 , that is the average output radiance is always smaller than the input radiance, being equal to it only when the internal wall is an ideal mirror and the input angular aperture is greater than the acceptance angle of the CPC (5°). This can be easily demonstrated considering that, for $\theta_m > \theta_{acc}^{coll}$, we have:

$$\tau_{dir}^{lamb}(\theta_m) \leq \sin^2 \theta_{acc}^{coll} / \sin^2 \theta_m \leq 1 \quad (12)$$

then Eq. (11) becomes:

$$C_{opt}^{lamb}(\theta_m) = \tau_{dir}^{lamb}(\theta_m) \cdot C_{geo} \cdot \sin^2 \theta_m \leq \sin^2 \theta_{acc}^{coll} \cdot C_{geo} \quad (11')$$

Considering that $1/\sin^2 \theta_{acc}^{coll}$ corresponds to the maximum value of the optical concentration ratio, equal to C_{geo} [1], from Eq. (11') we conclude that $C_{opt}^{lamb}(\theta_m) \leq 1$.

3.4. Analysis of the Flux Distribution on the Receiver

To study the flux transmitted to the exit aperture of the CPC, the exit aperture was closed by an ideal absorber. Fig. 9 shows the maps of the irradiance on the receiver as function of the angular aperture of the lambertian beam at input, from 1.0° to 6.0° ; the wall reflectivity is 1.0. Contrary to the maps obtained by irradiating the CPC with a parallel beam [2], the maps of Fig. 9 are symmetric respect to the optical axis, as consequence of the rotational symmetry of both the CPC and the lambertian beam. The optical simulations were performed by setting a number of input rays $N_{in}=100k$ for $\theta_m = 6.0^\circ$, then $N_{in}(\theta_m)$ is given by:

$$N_{in}(\theta_m) = \frac{\sin^2(\theta_m)}{\sin^2(6^\circ)} \cdot N_{in}(6^\circ) \quad (13)$$

The cross-section profiles of the output irradiance on the receiver of the CPC, simulated for two wall reflectivities, 1.0 and 0.9, are shown in Fig. 10. It can be seen that the flux is concentrated at first in the middle of the receiver ($\theta_m = 1.0^\circ$), then it is distributed in the central part ($\theta_m = 2.0^\circ$); at $\theta_m = 3.0^\circ$ the center is impoverished, but again, starting from $\theta_m = 3.5^\circ$ we have an almost uniform distribution of the flux in the central part of the receiver, which extends to the edge at increasing θ_m , to become uniform when θ_m reaches a value equal to the acceptance angle (5°). Then we can say that the flow affects at first the central part of the receiver and then the outer ring. In essence, the less inclined rays gather in the central part of the receiver, while those more inclined gather on its edge.

We can see from Fig. 10a, where the wall reflectivity is unitary and we have no optical losses inside the CPC, that the output irradiance profile becomes flat as soon as the angular aperture θ_m exceeds the acceptance angle (5.0°). By reducing R_w , the irradiance profiles are slightly smoothed, because of the optical loss inside the CPC; at the same time, they become blunt at the edges, because the optical loss is higher there as an effect of the higher number of reflections, as we will see shortly after.

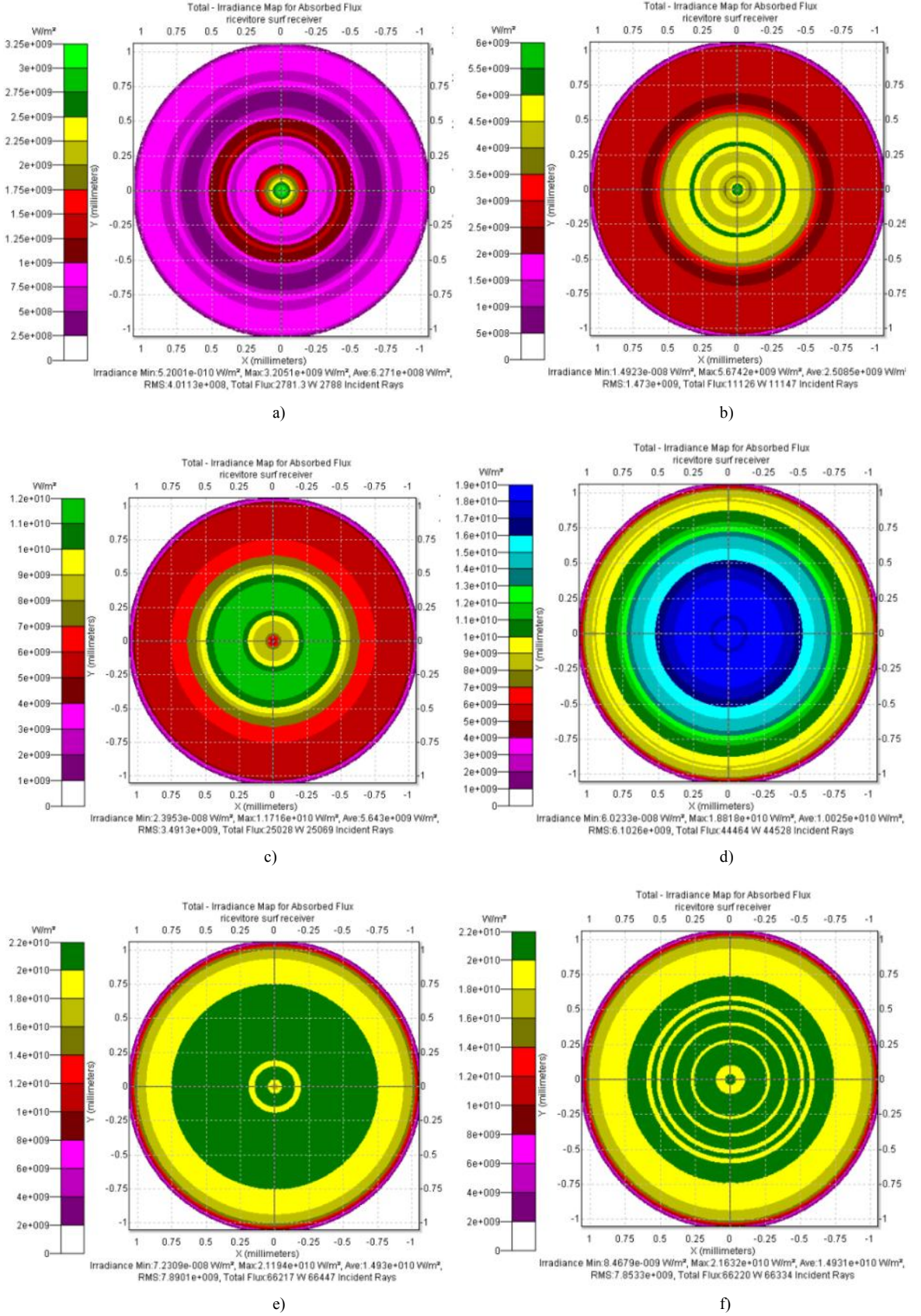


Figure 9. Maps of output flux on the receiver for different angular apertures of the lambertian beam at input: $\theta_m = 1.0^\circ$ (a); 2.0° (b); 3.0° (c); 4.0° (d); 5.0° (e); 6.0° (f). Number of input rays: 100k at $\theta_m = 6^\circ$. $R_w = 1.0$

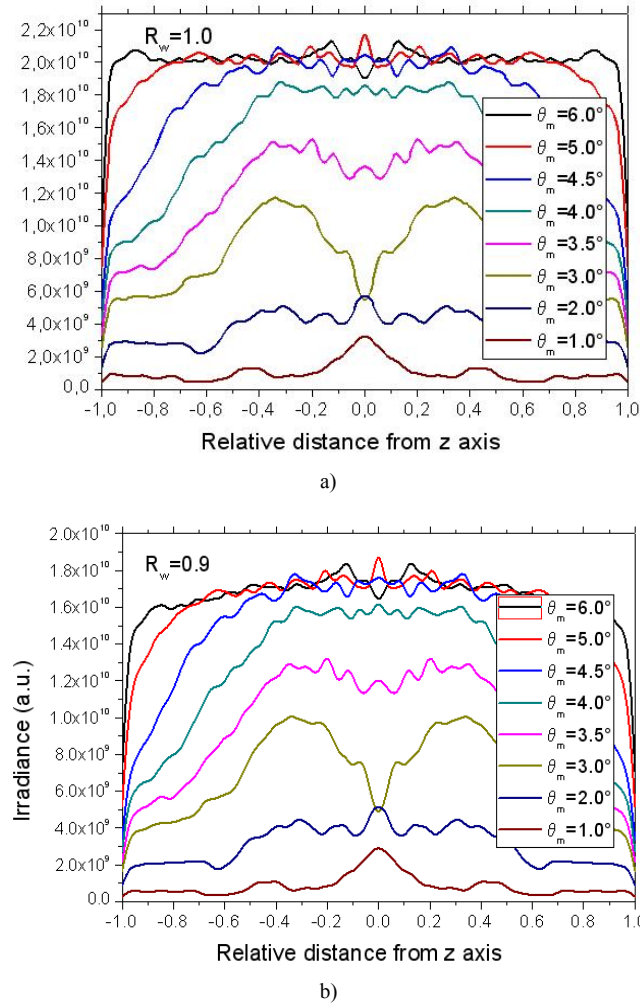


Figure 10. Irradiance profiles of the flux at output of the CPC, irradiated by a lambertian beam of different angular apertures θ_m . Wall reflectivity: $R_w = 1.0$ (a); $R_w = 0.9$ (b)

3.5. Average Number of Reflections of Locally Absorbed Rays

As done for the total flux transmitted to the receiver, we are able now to evaluate the average number of reflections experienced by the rays reaching a specific point on the receiver. We use therefore the same Eq. (9), to be applied to the irradiance profiles of transmitted flux, calculated for different values of the wall reflectivity. The irradiance is expressed as: $E(R_w, \theta_m, x)$, where x is the relative distance from the optical axis of the point on the receiver. The average number of reflections $\bar{N}(R'_w, R''_w, \theta_m, x)$ calculated for a specific value of θ_m can be therefore obtained from two simulations taken at different wall reflectivities, as follows:

$$\bar{N}(R'_w, R''_w, \theta_m, x) \approx \frac{\log \left[\frac{E(R'_w, \theta_m, x)}{E(R''_w, \theta_m, x)} \cdot \frac{N(R''_w, \theta_m)}{N(R'_w, \theta_m)} \right]}{\log \left[\frac{R'_w}{R''_w} \right]} \quad (14)$$

As the input beam is Lambertian, Eq. (14) gives the average number of reflections that the input rays, incident at angles in the $0^\circ \div \theta_m$ interval, experience before reaching a point on the receiver. As we are interested to know the average number of reflections done by the rays inclined in a narrow range $\Delta\theta_m$ centered at a particular θ_m value, we have calculated new irradiance profiles, $E(R_w, \Delta\theta_m, x)$, obtained as:

$$E(R_w, \Delta\theta_m, x) = E(R_w, \theta'_m, x) - E(R_w, \theta''_m, x) \quad (15)$$

where $\Delta\theta_m = \theta'_m - \theta''_m > 0$, and from these profiles we have obtained the searched result:

$$\bar{N}(R'_w, R''_w, \Delta\theta_m, x) \approx \dots \log \left[\frac{E(R'_w, \Delta\theta_m, x)}{E(R''_w, \Delta\theta_m, x)} \cdot \frac{N(R''_w, \Delta\theta_m)}{N(R'_w, \Delta\theta_m)} \right] \dots \approx \frac{\log \left[\frac{R'_w}{R''_w} \right]}{\log \left[\frac{R'_w}{R''_w} \right]} \quad (16)$$

Fig. 11 shows the curves of $\bar{N}(R'_w, R''_w, \Delta\theta_m, x)$ calculated for the five angular intervals: $\Delta\theta_m = 0^\circ-1^\circ$; $1^\circ-2^\circ$; $2^\circ-3^\circ$; $3^\circ-4^\circ$; $4^\circ-5^\circ$. The curves have a very interesting behavior. First of all, they overlap quite well, showing that the number of reflections of rays reaching a specific point at distance x , is only slightly dependent on the angular divergence at input. This is particularly true for middle values of x , less for the points at the center and at the edge of the receiver. The second consideration to do is that $\bar{N}(1.0, 0.9, \Delta\theta_m, x)$ is low at the center of the receiver, between about 1 and 2, and grows moving towards the edges, reaching values between about 3 and 5. This explains the statement made at the end of section 3.4.

As $\bar{N}(1.0, 0.9, \Delta\theta_m, x)$ is not too much dependent on θ_m , it is interesting to calculate its average respect to the different angular aperture intervals $\Delta\theta_m$. The average quantity $\bar{\bar{N}}(1.0, 0.9, x)$ is shown in Fig. 12 (black curve). It is a very smooth curve, no longer containing the strong oscillations of the curves of Fig. 11.

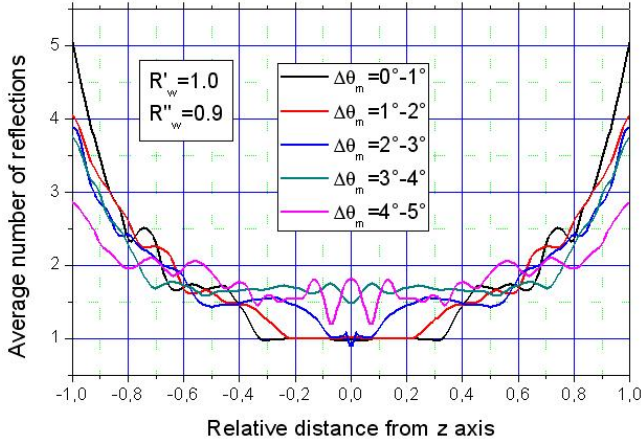


Figure 11. Average number of reflections of the rays incident at x relative distance from the optical axis on the exit aperture of the 3D-CPC, irradiated by a lambertian beam with different values of angular divergence $\Delta\theta_m$

$\bar{N}(1.0, 0.9, x)$ is well fitted by the fourth degree polynomial (see red curve in Fig. 12):

$$\bar{N}(1.0, 0.9, x) = a + b x^2 + c x^4 \quad (17)$$

with $a = 1.447$; $b = 0.2121$; $c = 1.703$.

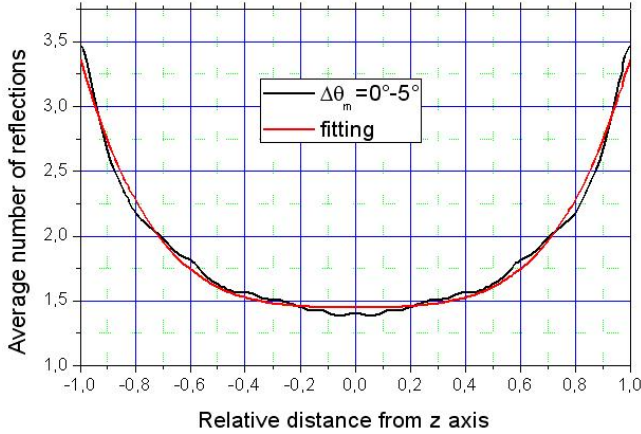


Figure 12. Average number of reflections of the rays incident at x distance from the optical axis on the exit aperture of the 3D-CPC, irradiated by a lambertian beam with angular divergence $\Delta\theta_m = 0^\circ-5^\circ$ (black curve). The red curve is the fitting polynomial

Fig. 13 (black curve) shows the average number of reflections $\bar{N}(R'_w, R''_w, \Delta\theta_m, x) = \bar{N}(1.0, 0.9, 0^\circ-1^\circ, x)$ simulated for an angular aperture of the lambertian beam equal to 1° . The curve shows that \bar{N} is exactly 1.0 in the central part of the receiver and increases with a step-like behavior moving towards the edge of the receiver, where the rays arrive after exactly 5 reflections. The rays at input are almost parallel to the optical axis, then the black curve of Fig. 13 is very similar to the red curve obtained in [2] when a collimated beam parallel to the optical axis irradiates the CPC. The difference between the two curves is very little: the red curve has a slightly larger zone with one reflection, and the number of reflections for the rays on the edge is now

seven.

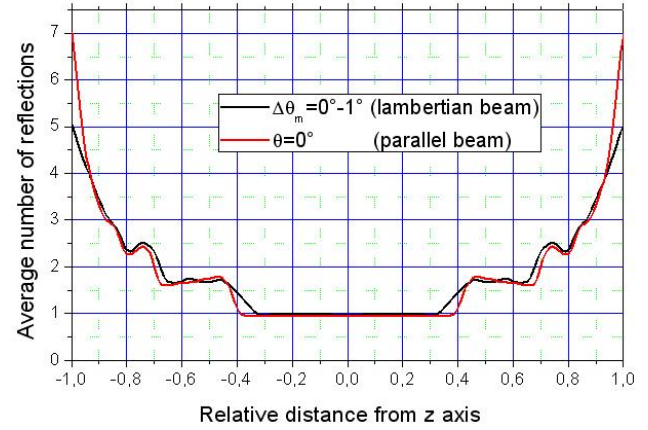


Figure 13. Average number of reflections of the rays incident on the receiver at x distance from the optical axis. The CPC is irradiated by a lambertian beam with angular divergence $\Delta\theta_m = 0^\circ-1^\circ$ (black curve) and by a collimated beam parallel to the optical axis of the CPC (red curve)

3.6. Angular Divergence of the Transmitted Rays

The study of the angular divergence of rays at output of the CPC is important to optimize the absorption properties of the receiver. In the practical use of a PV solar concentrator, for example, the receiver is not an ideal absorber, but a solar cell with specific reflectance properties, that affect its light absorption capabilities in relation to the divergence of the incoming rays [20]. The flux absorbed by the solar cell can be expressed as:

$$\Phi_{abs} \approx 2\pi \cdot A_{out} \cdot \dots \cdot \int_0^{\pi/2} d\theta_\tau \cdot \sin \theta_\tau \cdot \cos \theta_\tau \cdot L_{out}(\theta_\tau) \cdot (1 - R(\theta_\tau)) \quad (18)$$

where A_{out} is the area of the cell, $R(\theta_\tau)$ is the angle-resolved reflectance and $L_\tau(\theta_\tau)$ is the radiance of light transmitted at exit angle θ_τ by the CPC (the radiance is not function of the azimuthal angle ϕ_τ because the system input beam + CPC is rotationally symmetric).

In Eq. (18), in general $R(\theta_\tau)$ grows with θ_τ [20], then it is desirable that $L_\tau(\theta_\tau)$ be not too high for high θ_τ values. To check the angular distribution of radiance of light at the CPC receiver, we have irradiated the ideal CPC ($R_w = 1.0$) by a lambertian beam with different values of the angular aperture θ_m , and the output flux has been collected by a hemispherical absorber (radius $R_\tau = 200$ mm) centered on the receiver (see Fig. 14). The rotationally symmetric map of the flux density on the internal screen surface, projected on a plane orthogonal to the optical axis (see Fig. 16) and the corresponding radial profile, simulated at $\theta_m = 1^\circ$, are shown in Fig. 15.

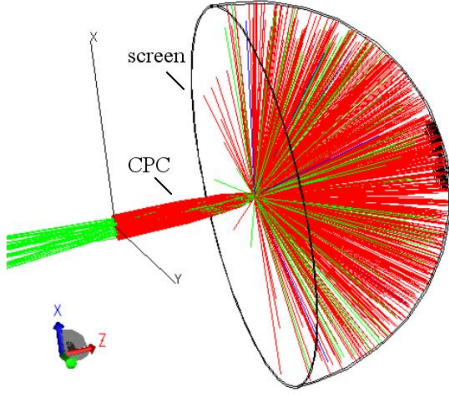
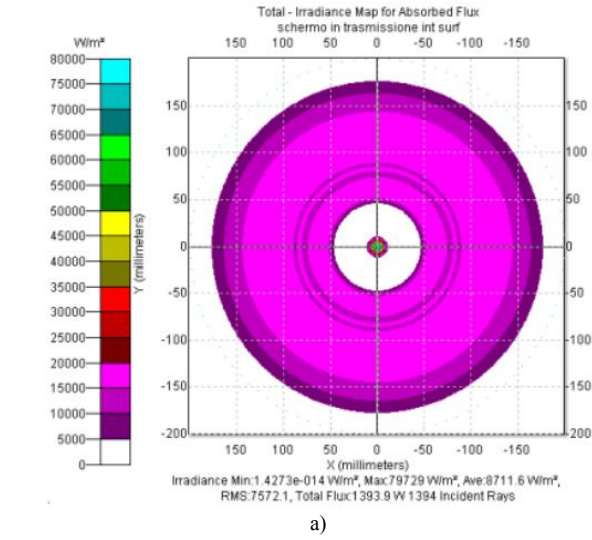
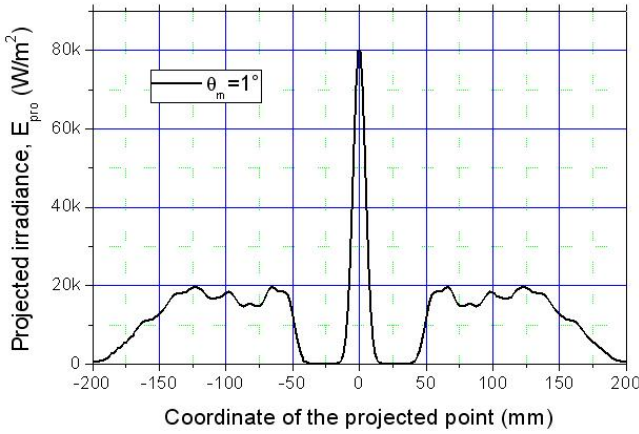


Figure 14. Scheme of the CPC irradiated by a lambertian beam with 5° angular aperture, $\theta_m = 5^\circ$. The transmitted rays are collected by a hemispherical screen with a radius $R_\tau = 200$ mm. Some of rays (green color) are back reflected and attenuated because the wall reflectivity is $R_w = 0.9$. Most of rays are transmitted and impact on the spherical screen; the red rays are less attenuated (lower number of reflections inside the CPC), whereas the green rays are more attenuated (higher number of reflections inside the CPC)



a)



b)

Figure 15. Map (a) and corresponding radial profile (b) of the flux density (irradiance) (in W/m^2) produced on the screen, projected over a plane orthogonal to the optical axis. The input is a lambertian beam with $\theta_m = 1^\circ$

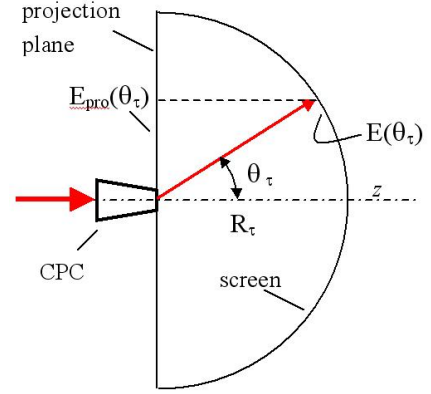


Figure 16. Schematic representation of the transmission of light to the spherical screen, the production of a flux density (irradiance) $E(\theta_\tau)$ on its internal wall and the projection of this irradiance, $E_{pro}(\theta_\tau)$, on a plane orthogonal to the optical axis

If $E(\theta_\tau)$ (W/m^2) is the irradiance on the screen surface, $E_{pro}(\theta_\tau)$ (W/m^2) is its projection on the orthogonal plane and $I_\tau(\theta_\tau)$ (W/sr) is the radiant intensity, the radiance $L_\tau(\theta_\tau)$ ($\text{W/m}^2\text{sr}$) of the transmitted light becomes:

$$L_\tau(\theta_\tau) = \frac{I_\tau(\theta_\tau)}{A_{out} \cdot \cos \theta_\tau} = \frac{R_\tau^2 \cdot E(\theta_\tau)}{A_{out} \cdot \cos \theta_\tau} = \dots$$

$$\dots = \frac{R_\tau^2}{A_{out}} \cdot E_{pro}(\theta_\tau) \quad (19)$$

where A_{out} is the area of the output aperture of the CPC and R_τ is the screen radius. From Eq. (19) we see that the profile of $E_{pro}(\theta_\tau)$, that reported in Fig. 15b, is the same of the radiance $L_\tau(\theta_\tau)$ (R_τ^2/A_{out} is a constant factor), and then the flux map of Fig. 15 is qualitatively the map of the transmitted radiance. The profile of $L_\tau(\theta_\tau)$ is worth of being analyzed in detail.

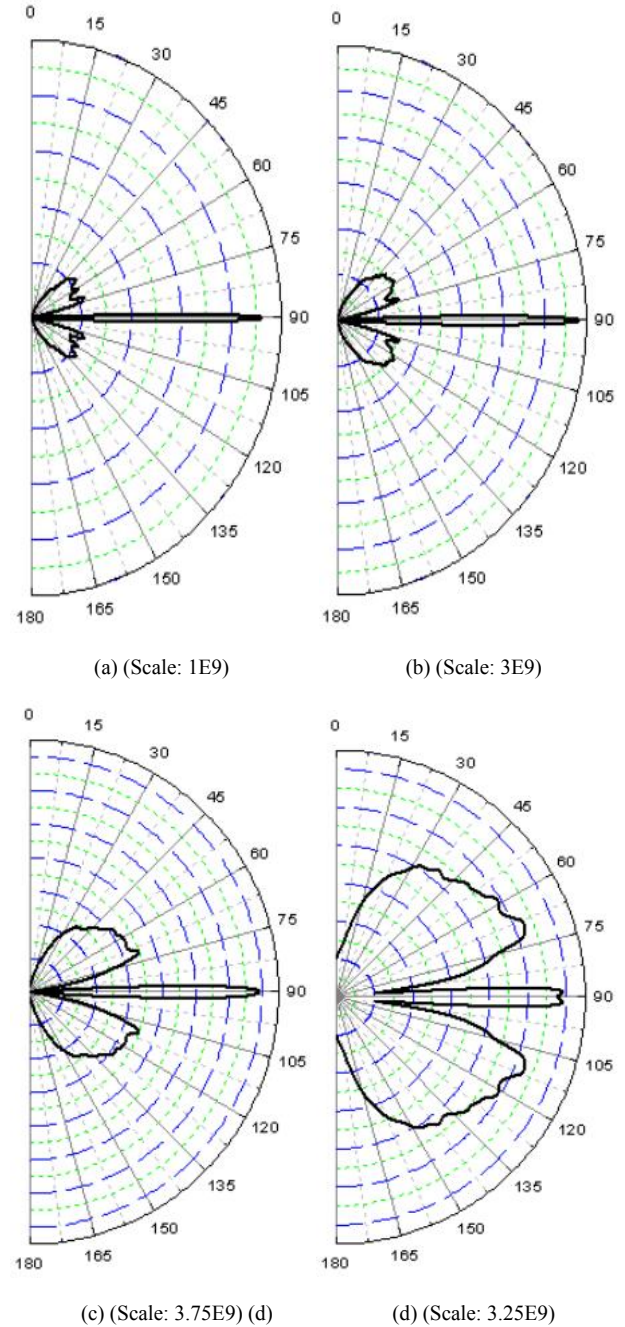
Fig. 17 shows the effect of the angular divergence θ_m on the angular distribution of radiance of the transmitted beam, for a wall reflectivity $R_w = 1.0$ (no optical loss by absorption). The number of rays incident at input aperture are a function of θ_m and follows the $\sin^2 \theta_m$ rule, which, in this case, corresponds to 50k at $\theta_m = 6^\circ$. The angular divergence θ_m was varied from 1° to 10° with 1° steps, but we show in Fig. 17 only the first six diagrams, because the polar profiles of $L_\tau(\theta_m, \theta_\tau)$ do not change significantly for $\theta_m > 6^\circ$, apart from small fluctuations at near $\theta_\tau = 0^\circ$. The radiance profiles show a strong central peak at $\theta_m < \theta_{acc}^{coll}$ values. This peak is mainly produced by rays

traveling close to the optical axis and crossing undisturbed the CPC without reflections on the internal wall. At $\theta_m < \theta_{acc}^{coll}$, we find a “dead” zone large $\approx 15^\circ$, with no rays, followed by a large band of radiance extending from about 15° to 60° , that takes, near the acceptance angle, the characteristic shape of a “butterfly” or “dragonfly”. The “dead” zone is very similar to that occurring with irradiation by a collimated beam parallel to the optical axis [2]. In that work, we could explain that the dead zone upper limit (about 15°) was due to those rays impacting on the CPC wall at about 7 mm far from the axis, and coming out with a divergence of about 15° ; this divergence is a lower limit, since away more from the axis, these rays undergo a second reflection that makes them diverge even more, and therefore makes it impossible exit angles of less than about 15° . Despite being the irradiation Lambertian, instead of parallel, this phenomenon is maintained, because the lambertian beam contains incoming parallel rays parallel or nearly parallel to the optical axis. When the input angular divergence θ_m reaches the acceptance angle (5°), the radiance profile is quite flat up to 75° (the small fluctuations depend only on the limited number of incident rays) and keeps almost equal up to $\theta_m = 10^\circ$. The same profile of transmitted radiance was achieved by increasing θ_m . Fig. 18a shows, for example, the transmitted radiance profile obtained at $\theta_m = 90^\circ$. The simulation was carried out with a flux of 400k rays (400k W) and a processing time of about 12 hours; the number of rays, however, was less than would have been necessary to satisfy the $\sin^2 \theta_m$ rule, which assures a constant radiance at input: $\sim 4.5\text{M}$ rays and ~ 130 hours of processing time. The consequence is a loss in the signal-to-noise ratio, as it can be seen in Fig. 18a.

Apart from the low signal-to-noise ratio, the simulation at $\theta_m = 90^\circ$ has not changed significantly the radiance profile found at 6° (see Fig. 17f) (we know in fact from [2], section 4.2, that input rays tilted more than $\approx 5.8^\circ$ have no chances to reach the CPC exit opening): a quite flat profile at $\sim 3.2 \cdot 10^9 \text{ W/m}^2\text{-sr}$ from 0° to 75° , followed by a decay up to $\sim 1.6 \cdot 10^9 \text{ W/m}^2\text{-sr}$ at 90° . Despite not flat up to 90° , this is effectively the profile obtained with a lambertian beam. This was verified by irradiating the hemispherical screen directly with a lambertian beam, after removing the CPC. The result is the profile of Fig. 18b, where the intensity drops to 50% of maximum at the exit angle of 90° .

The evolution of the radiance profiles as function of θ_m can be followed also transforming the radiance polar diagrams of Fig. 17 into Cartesian diagrams and overlapping them (see Fig. 19). I added also the $\theta_m = 90^\circ$ profile obtained at a reduced processing time (~ 11 times),

distinguishable for the low signal-to-noise ratio. Apart from the radiance peak near $\theta_r = 0^\circ$ that we have already discussed, we see that the radiance profile monotonically grows in the $\Delta\theta_r \sim 15^\circ\text{-}80^\circ$ interval at increasing θ_m from 1° to 4° . A significant change in the radiance profile happens in the $\Delta\theta_m = 4^\circ\text{-}5^\circ$ interval, where we observe the filling of the dead zone at low θ_r values, as well as of the region between $\sim 20^\circ$ and $\sim 75^\circ$; the $75^\circ\text{-}90^\circ$ interval remains unfilled as explained before.



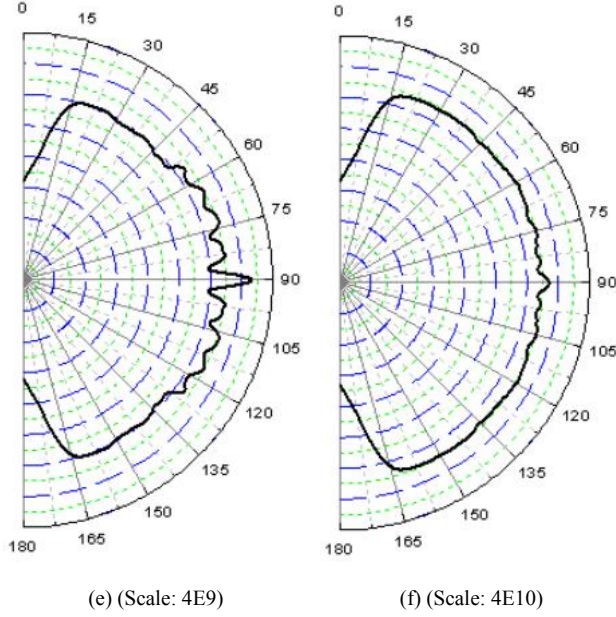


Figure 17. Polar representation of the distribution of the radiance of the transmitted flux, when the CPC is irradiated with a lambertian beam with angular divergence $\theta_m = 1^\circ$ (a); 2° (b); 3° (c); 4° (d); 5° (e); 6° (f). For the angular divergence $\theta_m = 6^\circ$ (f), We have used 500k rays at input, 10 times more than required to follow the $\sin^2 \theta_m$ rule. The scale of radiance is expressed in $\text{W/m}^2\text{sr}$ and is reported near each figure. The wall reflectivity is constant and equal to 1.0

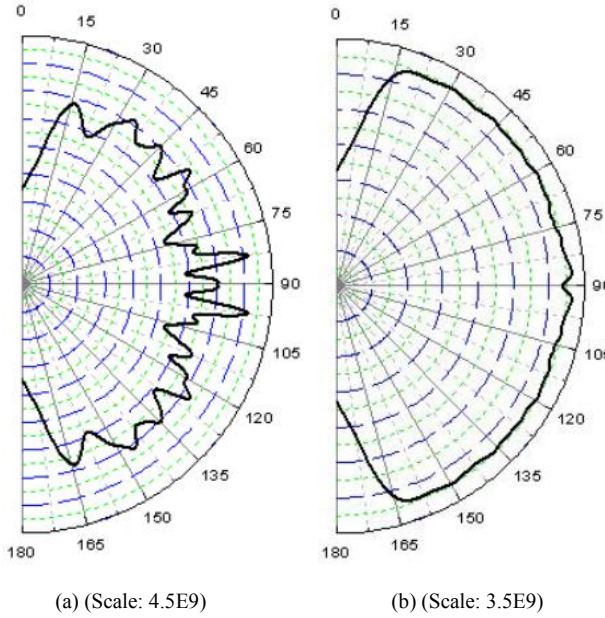


Figure 18. Polar radiance of the transmitted flux by the CPC irradiated with a lambertian beam. (a) Angular divergence $\theta_m = 90^\circ$, 400k rays at input, ~ 11 times less than required to follow the $\sin^2 \theta_m$ rule. (b) Angular divergence $\theta_m = 90^\circ$, 500k rays projected on the hemispherical screen directly, without the presence of the CPC. The wall reflectivity is 1.0. The scale of radiance is expressed in $\text{W/m}^2\text{sr}$

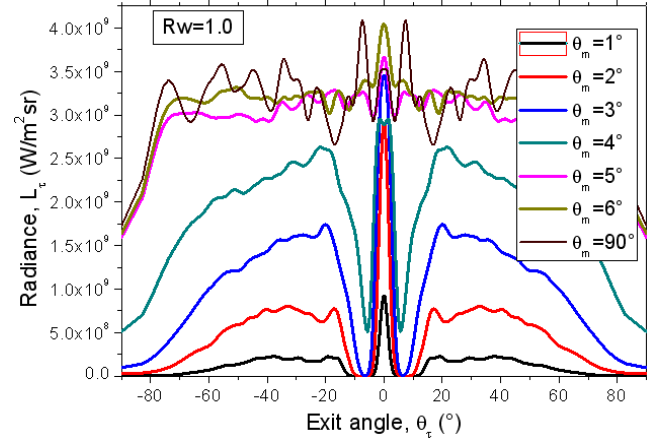
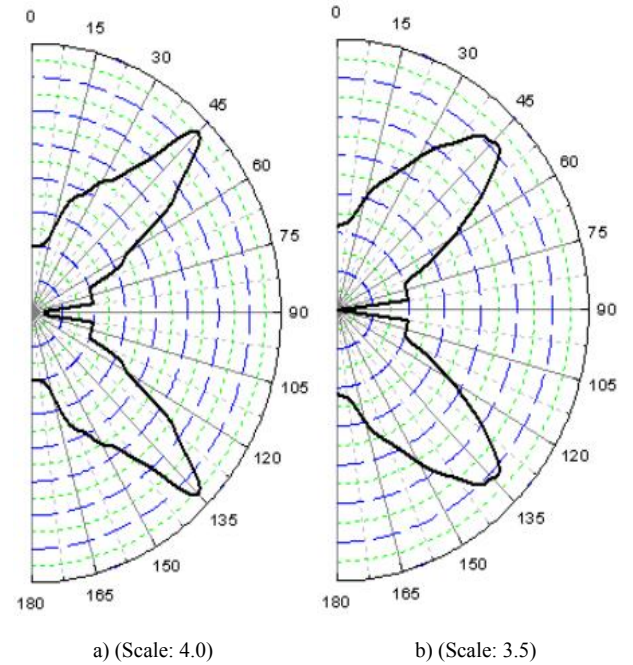


Figure 19. Cartesian representation of the distribution of the radiance of transmitted flux, when the CPC is irradiated with a lambertian beam with angular divergence $\theta_m = 1^\circ$; 2° ; 3° ; 4° ; 5° ; 6° ; 90° . The wall reflectance is constant and equal to 1.0

3.7. Average Number of Reflections of Transmitted Rays

We have previously analyzed the number of reflections made by the transmitted rays as function of θ_m , both as an average on the total flux, and as function on the distance, from the optical axis, of the impact point on the receiver. Now we look at the average number of reflections made by rays transmitted as function of the exit angle θ_τ from the CPC, at different values of the input lambertian divergence θ_m . For this purpose, we have repeated the simulations of radiance shown in Fig. 17 with a different wall reflectance, $R_w = 0.9$.



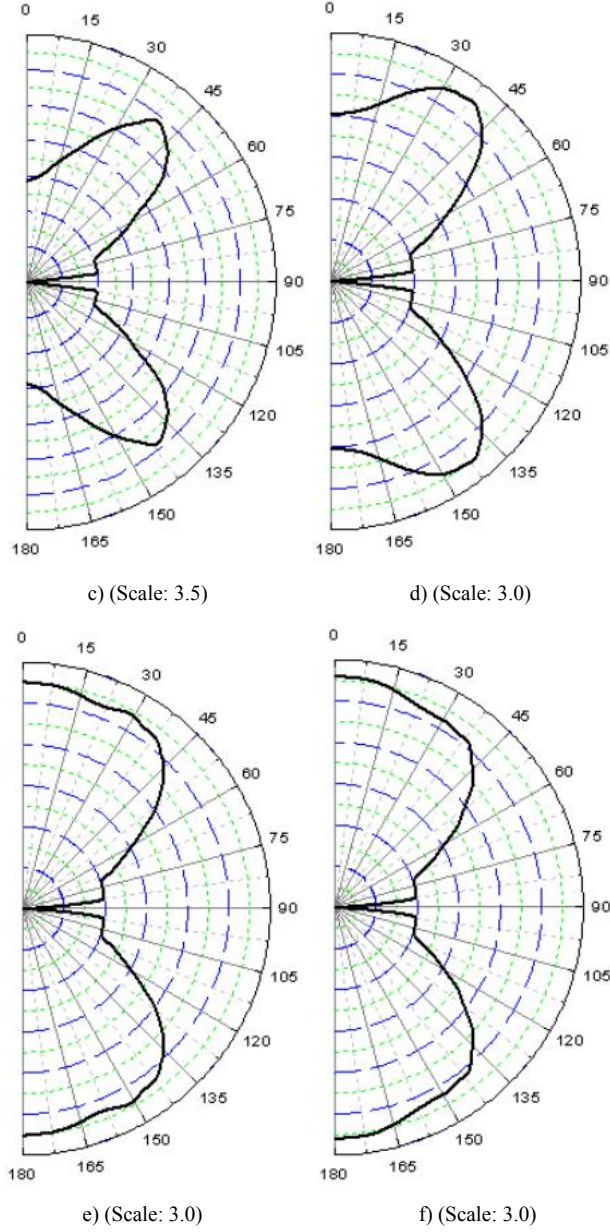


Figure 20. Polar maps of the average number of reflections of the transmitted rays as function of the exit angle θ_τ at different values of the Lambertian angular divergence θ_m : 1° (a); 2° (b); 3° (c); 4° (d); 5° (e); 6° (f)

The average number of reflections was obtained by applying the following equation, with $R'_w = 1.0$ and $R''_w = 0.9$:

$$\bar{N}(R'_w, R''_w, \theta_m, \theta_\tau) \approx \frac{\log \left[\frac{L_\tau(R'_w, \theta_m, \theta_\tau)}{L_\tau(R''_w, \theta_m, \theta_\tau)} \right]}{\log \left[\frac{R'_w}{R''_w} \right]} \quad (20)$$

where $L_\tau(R_w, \theta_m, \theta_\tau)$ is the radiance of the flux transmitted at angle θ_τ . The numbers of output rays do not appear as they were the same at the two wall reflectivities. Fig. 20 shows the polar distribution of $\bar{N}(\theta_m, \theta_\tau)$ for angular divergence values $\theta_m = 1^\circ \div 6^\circ$, with 1° steps. There are many interesting features of the polar diagrams of $\bar{N}(\theta_m, \theta_\tau)$ to highlight. First of all they are completely developed at $\theta_m = 5^\circ = \theta_{acc}^{coll}$, as it was for the radiance maps (Fig. 17). Then we notice that $\bar{N}(\theta_m, \theta_\tau) = 0$ for exit rays close to the optical axis ($\theta_\tau \leq 7^\circ$); these rays do not touch the CPC wall. Then, from $\theta_\tau \sim 7^\circ$ to $\theta_\tau \sim 22^\circ$, $\bar{N}(\theta_m, \theta_\tau)$ is exactly 1. At higher values of θ_τ , $\bar{N}(\theta_m, \theta_\tau)$ grows forming a lobe centered at $\sim 45^\circ$, which is narrow at low θ_m values, with a peak at $\bar{N}_{max} \approx 4$ for $\theta_m = 1^\circ$ and $\bar{N}_{max} = 3$ for $\theta_m = 2^\circ - 3^\circ$. The lobe then widens occupying the whole range from $\sim 45^\circ$ to 90° . At $\theta_m = 1^\circ$, the rays exit the CPC at $\theta_\tau = 90^\circ$ after one reflection; by increasing θ_m , the reflections increase up to 2.75. One last consideration to do is about the value of $\bar{N}(\theta_m, \theta_\tau)$. Whereas the number of reflections of a ray must be exactly an integer, this rarely happens to a mixture of rays, because they have not the same characteristics (same distance x at input aperture and same θ_m). Exceptions are $\bar{N}(\theta_m, \theta_\tau) = 1$ at all θ_m when $\theta_\tau \sim 7^\circ \div 22^\circ$ (see Figs. 20a-f), or at $\theta_m = 1^\circ \div 2^\circ$ when $\theta_\tau = 90^\circ$ (see Figs. 20a,b), or again $\bar{N}(\theta_m, \theta_\tau) = 3$ at $\theta_m = 2^\circ \div 3^\circ$ when $\theta_\tau \sim 45^\circ$ (see Figs. 20b,c). The diagrams of radiance of Fig. 17 and those of the average number of reflections of Fig. 20 do not clarify, therefore, what are, at the origin, the rays causing a particular radiance or number of reflections profile.

To improve the analysis of the average number of reflections of the transmitted rays, we divided the θ_m interval ($0^\circ - 5^\circ$) in five smaller intervals $\Delta\theta_m = (0^\circ - 1^\circ)$; $(1^\circ - 2^\circ)$; $(2^\circ - 3^\circ)$; $(3^\circ - 4^\circ)$; $(4^\circ - 5^\circ)$, with $\Delta\theta_m = \theta''_m - \theta'_m$. The formula used to calculate the number of reflections is:

$$\begin{aligned} \bar{N}(R'_w, R''_w, \Delta\theta_m, \theta_\tau) &= \dots \\ &= \frac{\log \left[\frac{L_\tau(R'_w, \theta''_m, \theta_\tau) - L_\tau(R'_w, \theta'_m, \theta_\tau)}{L_\tau(R''_w, \theta''_m, \theta_\tau) - L_\tau(R''_w, \theta'_m, \theta_\tau)} \right]}{\log \left[\frac{R'_w}{R''_w} \right]} \quad (21) \end{aligned}$$

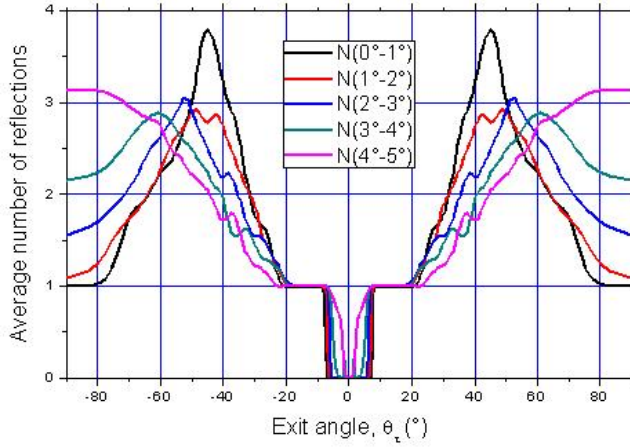


Figure 21. Cartesian representation of the average number of reflections of the transmitted rays for an input lambertian beam with angular divergence in the intervals: $\Delta\theta_m = (0^\circ-1^\circ)$ (black); $(1^\circ-2^\circ)$ (red); $(2^\circ-3^\circ)$ (blue); $(3^\circ-4^\circ)$ (dark cyan); $(4^\circ-5^\circ)$ (magenta)

The radiance profiles $L_\tau(R_w, \theta_m, \theta_\tau)$ are those previously simulated with $R'_w = 1.0$ and $R''_w = 0.9$. Eq. (21) only requires subtraction of radiance profiles with different R_w values. The obtained profiles of $\bar{N}(1.0, 0.9, \Delta\theta_m, \theta_\tau)$ are reported, in Cartesian representation, in Fig. 21, which allows to distinguish better the transmitted rays. Fig. 21 confirms that $\bar{N} = 0$ for $\theta_\tau < 7.5^\circ$ and that $\bar{N} = 1$ for $\Delta\theta_\tau = 7.5^\circ \div 22^\circ$. We note also that the various \bar{N} profiles consist of bands with the maximum on integer values of \bar{N} , as desired. The position of these bands (θ_b) and their maximum value \bar{N}_b are reported in Tab. 1, as function of $\Delta\theta_m$.

Table 1. Features of \bar{N} profiles. The bands \bar{N}_b , with angular position

θ_b are reported as function of the $\Delta\theta_m$ interval

$\Delta\theta_m$ (°)	\bar{N}_b	θ_b (°)
0-1	≈ 4 (3.8)	45
	1	80-90
1-2	≈ 3 (2.9)	46
	1	80-90
2-3	3	52
	1.5	90
3-4	≈ 3 (2.9)	61
	≈ 2 (2.1)	90
4-5	≈ 3 (3.1)	75-90

4. Analysis of the Reflected Flux

4.1. Optical Reflection Efficiency

Let us consider at first the total reflected flux:

$$\begin{aligned} \Phi_\rho &= \Phi_{in} \cdot \rho_{dir}^{lamb}(R_w, \theta_m) = \Phi_{in} - \Phi_\alpha - \Phi_\tau = \dots \\ &\dots = \Phi_{in} \cdot [1 - \alpha_{dir}^{lamb}(R_w, \theta_m) - \tau_{dir}^{lamb}(R_w, \theta_m)] \end{aligned} \quad (22)$$

where Φ_α and Φ_τ are the total absorbed and transmitted fluxes, respectively, and $\rho_{dir}^{lamb}(R_w, \theta_m)$, $\alpha_{dir}^{lamb}(R_w, \theta_m)$, $\tau_{dir}^{lamb}(R_w, \theta_m)$ are the lambertian reflection, absorption and transmission efficiencies, respectively. The total reflected flux can be expressed as function of the radiance $L_\rho(R_w, \theta_m, \theta_\rho)$ of the reflected light:

$$\Phi_\rho(R_w, \theta_m) = \dots \quad (23)$$

$$= A_{in} \cdot 2\pi \int_0^{\pi/2} d\theta_\rho \cdot \sin \theta_\rho \cdot \cos \theta_\rho \cdot L_\rho(R_w, \theta_m, \theta_\rho)$$

where θ_ρ is the polar angle of the reflected ray. To simulate the reflection properties of the CPC, we have adopted a scheme similar to that used to measure the transmitted light (see Figs. 14, 16), adding a hemispherical screen with $R_\rho = 1000$ mm radius and ideal absorbance, able to gather all the reflected light from the CPC. The CPC protrudes out of the screen and the center of input aperture meets that of the screen (see Fig. 22).

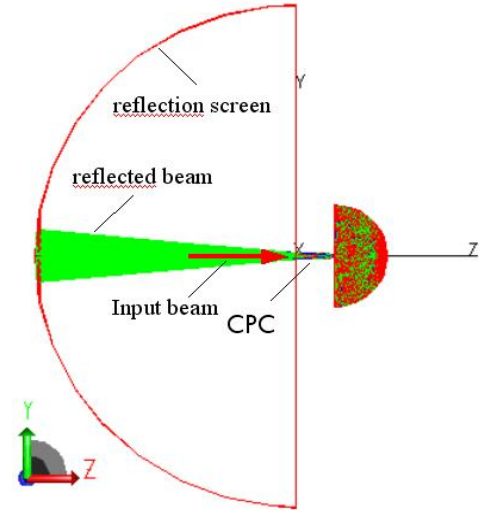


Figure 22. Scheme of the 3D-CPC irradiated by a lambertian beam with angular divergence θ_m . The reflected flux is measured by an absorbing hemispherical screen of radius $R_\rho = 1000$ mm. The CPC of the figure is not ideal ($R_w = 0.9$), as consequence, the incident rays (red color) are attenuated after reflection (green color). The output of the CPC has been left open, so the transmitted rays are visible. Most of the transmitted rays are attenuated (green color); the red beam on the z -axis is made of rays crossing undisturbed the CPC

The optical reflection efficiency is defined as the ratio of the output reflected flux to the input flux:

$$\rho_{dir}^{lamb}(R_w, \theta_m) = \frac{\Phi_\rho(R_w, \theta_m)}{\Phi_{in}} \quad (24)$$

Fig. 23 shows the curve of reflection efficiency calculated for $R_w = 1.0$ (black curve), condition for which ρ_{dir}^{lamb} is equal to the ratio between the number of the back-reflected rays to the input rays, because of the absence of optical loss inside the CPC. The reflection efficiency is zero below the acceptance angle, as all the rays are transmitted; then it appears in correspondence of θ_{acc}^{coll} (see red curve).

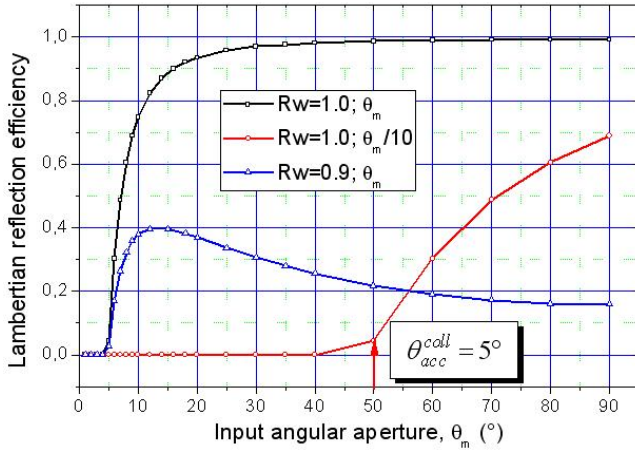


Figure 23. Lambertian reflection efficiency $\rho_{dir}^{lamb}(R_w, \theta_m)$ of the 3D-CPC calculated for $R_w = 1.0$ and 0.9 wall reflectivity. A portion of the curve of $\rho_{dir}^{lamb}(1.0, \theta_m)$ is also shown vs. $\theta_m/10$ (x axis scaled by a factor of 10)

The growth of $\rho_{dir}^{lamb}(R_w, \theta_m)$ for $R_w = 1.0$ is easily obtained considering that it is simply the complement to 1 of the transmission efficiency $\tau_{dir}^{lamb}(R_w, \theta_m)$ when $\theta_m \geq \theta_{acc}^{coll}$ (see Eq. (7)). We have therefore:

$$\rho_{dir}^{lamb}(1.0, \theta_m) = 1 - \tau_{dir}^{lamb}(1.0, \theta_m) = 1 - \frac{\sin^2 \theta_{acc}^{coll}}{\sin^2 \theta_m} \quad (25)$$

The evolution of $\rho_{dir}^{lamb}(1.0, \theta_m)$ vs. θ_m is quite different from that of $\eta_\rho(1.0, \theta_{in})$, the reflection efficiency relative to a parallel beam [2]; in that case it was growing rapidly before the acceptance angle, reaching half of its maximum just in correspondence of it. With a lambertian beam, $\rho_{dir}^{lamb}(1.0, \theta_m)$ is growing more slowly (see Fig. 23) because a part of the beam, that corresponding to $\theta_m = \theta_{acc}^{coll}$, is always transmitted. From Eq. (25) we see that the

limit of $\rho_{dir}^{lamb}(1.0, \theta_m)$, for $\theta_m = 90^\circ$, is: $1 - \sin^2 \theta_{acc}^{coll} \approx 0.992$. The reflection efficiency data relative to $R_w = 0.9$ are shown in Fig. 23 (blue curve). While the curve of $\rho_{dir}^{lamb}(1.0, \theta_m)$ is always growing, the curve of $\rho_{dir}^{lamb}(0.9, \theta_m)$ reaches a maximum at $\theta_m \approx 14^\circ$ and then decreases down to 16% for $\theta_m = 90^\circ$, being strongly limited by the absorbance of light on the CPC wall.

4.2. Angular Divergence of the Reflected Rays

The study of the angular divergence of back reflected rays from input aperture has not a practical relevance as it has in the case of the transmitted rays, but it is a useful exercise to apply also to the back reflected rays concepts of the theory of solar concentrators. To simplify the discussion, we limit ourselves to consider an ideal CPC ($R_w = 1$). As already seen discussing the transmitted flux, the TracePro software produces on the collecting screen a flux map corresponding to the irradiance on the screen wall projected on a plane orthogonal to the z axis. Apart from a dimensional constant factor, equal to R_ρ^2 / A_{in} , with $R_\rho = 1000$ mm radius of the screen and A_{in} input aperture of the CPC, this map is equivalent to that of the radiance of light back reflected by the input aperture, as it has been demonstrated in Eq. (19) for the transmitted flux. The plot of these maps is not necessary, because they are symmetric with respect to the optical axis, and then they give the same information of the profiles of their cross sections.

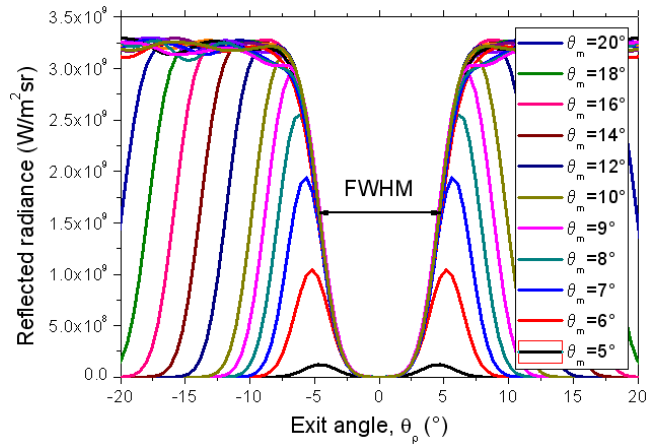


Figure 24. Profiles of the reflected radiance vs. the exit reflection angle θ_ρ , simulated for some values of θ_m from 5° to 20° . The envelope profile gives a reversed band due to the loss by transmitted rays and its FWHM $\approx 2 \times 4.5^\circ$. The wall reflectivity is 1.0

A Cartesian representation of the reflected radiance simulated for some values of $\theta_m \geq \theta_{acc}^{coll}$ up to $\theta_\rho = 20^\circ$ is shown in Fig. 24. The reflected radiance appears at $\theta_{acc}^{coll} = 5^\circ$ and then grows in intensity reaching a maximum of about 3.2×10^9 (W/m²sr) at around 12° . Keeping constant in

intensity, the radiance band expands then in terms of angular divergence. The envelope of all profiles corresponds to the radiance profile at $\theta_m = 90^\circ$, and is characterized by a depression in the center, caused by the “loss” by transmitted rays. This profile, if overturned, form a band of 3.2×10^9 ($\text{W}/\text{m}^2\text{sr}$) intensity and a width FWHM $\approx 2 \times 4.7^\circ$. This band definitely has to do with the missing transmitted rays, but it is unexpected that it is equal to $\approx 2 \times 4.5^\circ$ instead of being $2 \times \theta_{acc}^{coll} = 2 \times 5^\circ$.

The simulations were made throughout the angular range from 5° to 90° . In Fig. 25 the center of the radiance bands θ_p and their full width at half maximum $\Delta\theta = \theta_2 - \theta_1$ is reported as function of θ_m . The evolution of θ_p is perfectly linear and is defined by:

$$\theta_p(R_w, \theta_m) = \theta_p(1.0, \theta_m) = 2.24 + 0.5 \cdot \theta_m \quad (26)$$

The evolution of $\Delta\theta$ is different; after a slow rising up to 10° , the behavior becomes linear and is defined by the function:

$$\Delta\theta(R_w, \theta_m) = \Delta\theta(1.0, \theta_m) = -4.91 + 1.0 \cdot \theta_m \quad (27)$$

The upper value of polar angle of the reflected light is:

$$\theta_2 = \theta_p + \frac{\Delta\theta}{2} = \theta_m - 0.2 \approx \theta_m \quad (28)$$

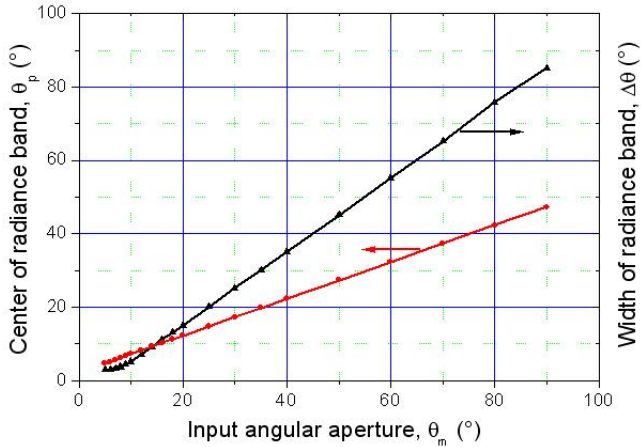


Figure 25. Center of the radiance bands θ_p and their full width at half maximum $\Delta\theta$ as function of θ_m

The maximum value of the exit angle, θ_2 , therefore, is almost equal to the maximum entrance angle, θ_m . This result is a direct consequence of the Liouville theorem [6], establishing the invariance of the “generalized étendue”, the volume occupied by the system in the phase space, as expressed by Eq. (29) (see also Fig. 26):

$$n^2 \cdot A \cdot \sin^2 \theta = (n')^2 \cdot A' \cdot \sin^2 \theta' = \text{const} \quad (29)$$

In our case the incident and reflected rays are in air ($n, n' =$

1) and cross the same port, the input aperture of area A_{in} , then we have:

$$A_{in} \cdot \sin^2 \theta_{in} = A_{in} \cdot \sin^2 \theta_{out} \Rightarrow \theta_{in} = \theta_{out} \quad (30)$$

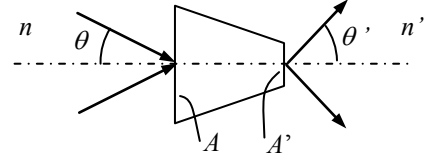
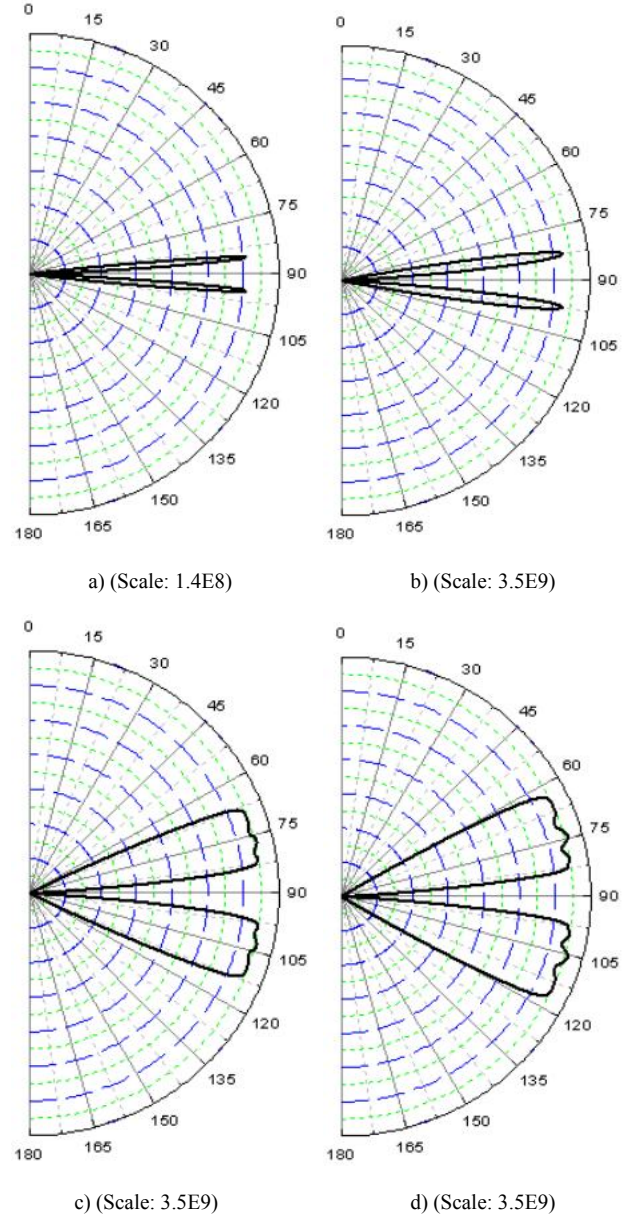


Figure 26. Scheme of a generic concentrator with the three main parameters for the input and output apertures: index of refraction, area and angular divergence

The polar diagrams of the angular distribution of reflected radiance are reported in Fig. 27 and are distributed throughout the angular range from 5° to 90° .



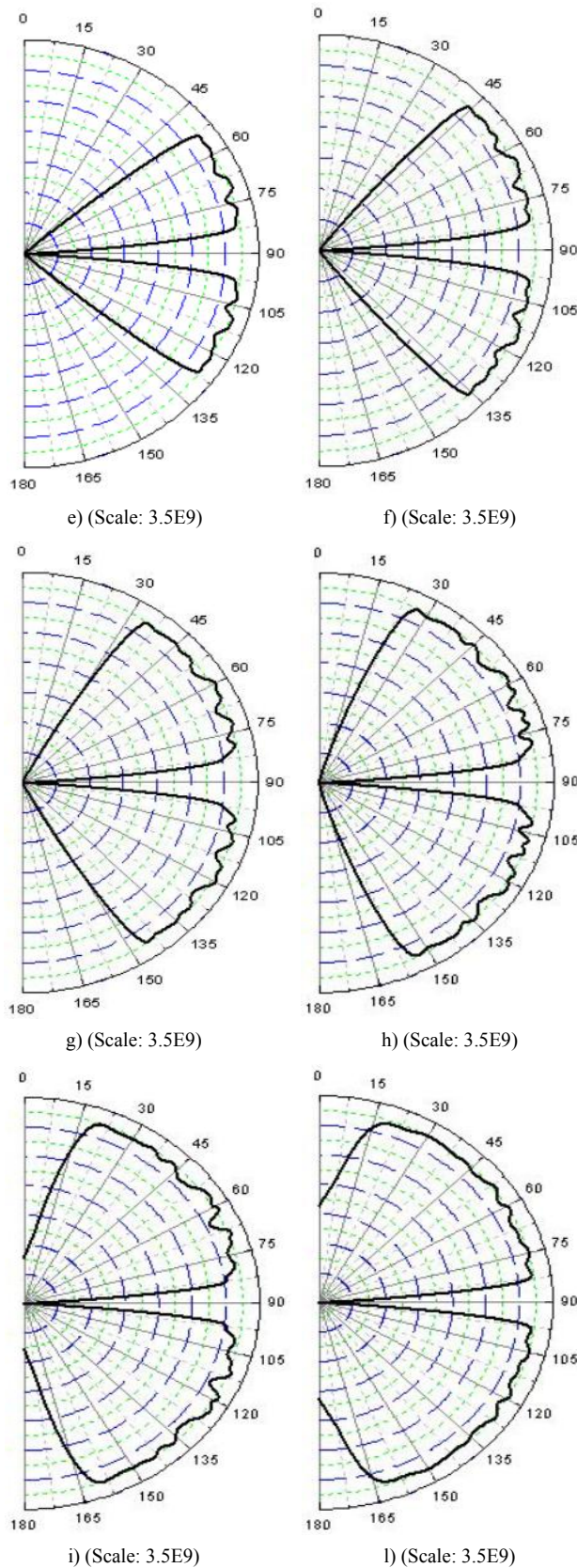


Figure 27. Polar diagrams of the angular distribution of the reflected radiance, simulated for different values of the angular aperture of the lambertian beam at input: $\theta_m = 5^\circ$ (a); 10° (b); 20° (c); 30° (d); 40° (e); 50° (f); 60° (g); 70° (h); 80° (i); 90° (l). The scale of radiance is expressed in $\text{W/m}^2\text{sr}$

As it can be seen in Fig. 27, the reflected light is a beam with the shape of a hollow cone, including an internal wall with semi-opening $\approx \theta_{acc}$, and an external wall with semi-opening equal to the angular aperture of the lambertian beam θ_m . Cross sections of these beams are then rings with the inner circle growing, at increasing θ_m , from 5° to 12° , and the outer circle from 5° to 90° .

4.3. Average Number of Reflections of the Total Reflected Rays

To derive the average number of reflections of the total reflected flux, $\bar{N}_\rho(R'_w, R''_w, \theta_m)$, it is sufficient to analyze the lambertian reflectance $\rho_{dir}^{lamb}(R_w, \theta_m)$ at two wall reflectivities and using the formula:

$$\bar{N}_\rho(R'_w, R''_w, \theta_m) \approx \frac{\log \left[\frac{\rho_{dir}^{lamb}(R'_w, \theta_m)}{\rho_{dir}^{lamb}(R''_w, \theta_m)} \cdot \frac{N_\rho(R''_w, \theta_m)}{N_\rho(R'_w, \theta_m)} \right]}{\log \left[\frac{R'_w}{R''_w} \right]} \quad (31)$$

where $N_\rho(R_w, \theta_m)$ is the number of reflected rays collected by the screen. The reflection efficiency functions used are those calculated at $R_w = 1.0$ and $R_w = 0.9$ (see Fig. 23).

Fig. 28 shows the curve of $\bar{N}_\rho(1.0, 0.9, \theta_m)$, obtained applying Eq. (31) to the pair of reflectivities (1.0; 0.9). The average number of reflections is four at near the acceptance angle (5°) and then grows monotonically reaching up to 16 reflections for $\theta_m = 90^\circ$.

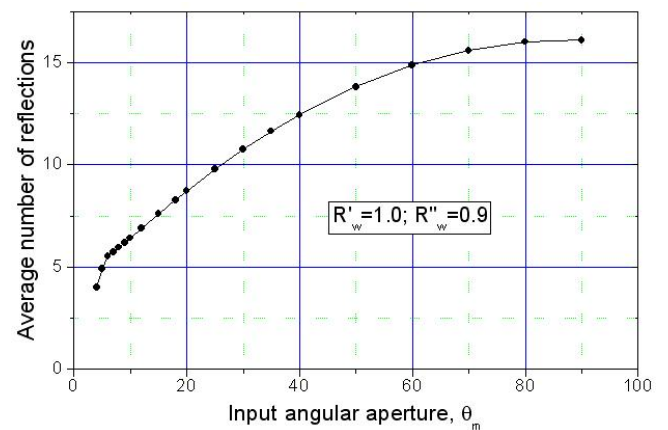


Figure 28. Average number of internal reflections of the back reflected rays, simulated by applying Eq. (31) for the pair of values of internal wall reflectivity: $(R'_w, R''_w) = (1.0; 0.9)$

4.4. Average Number of Reflections Associated to the Reflected Radiance

As we have done with the transmitted flux, the number of

internal reflections of the reflected rays, as function of the exit angle θ_ρ at different values of the angular aperture θ_m , can be calculated by simulating the radiance shown in Fig. 27 with a different wall reflectance, $R_w = 0.9$.

The average number of reflections $\bar{N}_\rho(R'_w, R''_w, \theta_m, \theta_\rho)$, with $R'_w = 1.0$ and $R''_w = 0.9$, was obtained by applying the following equation:

$$\bar{N}_\rho(R'_w, R''_w, \theta_m, \theta_\rho) \approx \dots$$

$$\log \left[\frac{L_\rho(R'_w, \theta_m, \theta_\rho)}{L_\rho(R''_w, \theta_m, \theta_\rho)} \cdot \frac{N_\rho(R''_w, \theta_m)}{N_\rho(R'_w, \theta_m)} \right] \quad (32)$$

$$\dots \approx \frac{\log \left[\frac{R'_w}{R''_w} \right]}{\log \left[\frac{R'_w}{R''_w} \right]}$$

where $L_\rho(R_w, \theta_m, \theta_\rho)$ is the radiance of the flux reflected at θ_ρ angle and $N_\rho(R_w, \theta_m)$ is the number of total reflected rays. The average number of internal reflections of the rays reflected at θ_ρ angle is shown in Fig. 29a for $\theta_m = 5^\circ, 6^\circ, 8^\circ, 10^\circ, 12^\circ, 18^\circ, 20^\circ$, and in Fig. 29b for $\theta_m = 30^\circ, 40^\circ, 50^\circ, 60^\circ, 70^\circ, 80^\circ, 90^\circ$. It is interesting to note that, apart from the curve corresponding to $\theta_m = 5^\circ$, all other curves have a characteristic “V” shape with a minimum of \bar{N}_ρ equal to ≈ 5 on the direction of the optical axis of the CPC, and a maximum of \bar{N}_ρ that grows at increasing θ_m and falling approximately at $\theta_\rho \approx \theta_m$.

The results of Fig. 29 are very plausible: the higher the angular divergence of the incoming beam, the greater the number of reflections that the rays experience within the CPC, the greater the exit angle of the rays that make the maximum number of internal reflections. It is also interesting to note that, for exit angles $\theta_\rho < \theta_m$, all the curves show an increasing trend of $\bar{N}_\rho(\theta_\rho)$ that is almost linear, particularly for high values of θ_m (see Fig. 29b). An exception to what has been said so far makes the curve corresponding to $\theta_m = 5^\circ$. It shows a constant trend $\bar{N}_\rho(\theta_\rho) = 5$ for $\theta_\rho < \theta_m$ (θ_{acc}^{coll}), but then decreases with increasing of θ_ρ over the value of θ_m , as do all the other curves. With regard to the values of $\bar{N}_\rho(\theta_m, \theta_\rho)$, they range from about 5 to about 30 and grow at growing θ_m , as illustrated in Fig. 28. Finally, Fig. 30 shows two examples of polar representation of $\bar{N}_\rho(\theta_m, \theta_\rho)$ for $\theta_m = 5^\circ$ and 90° .

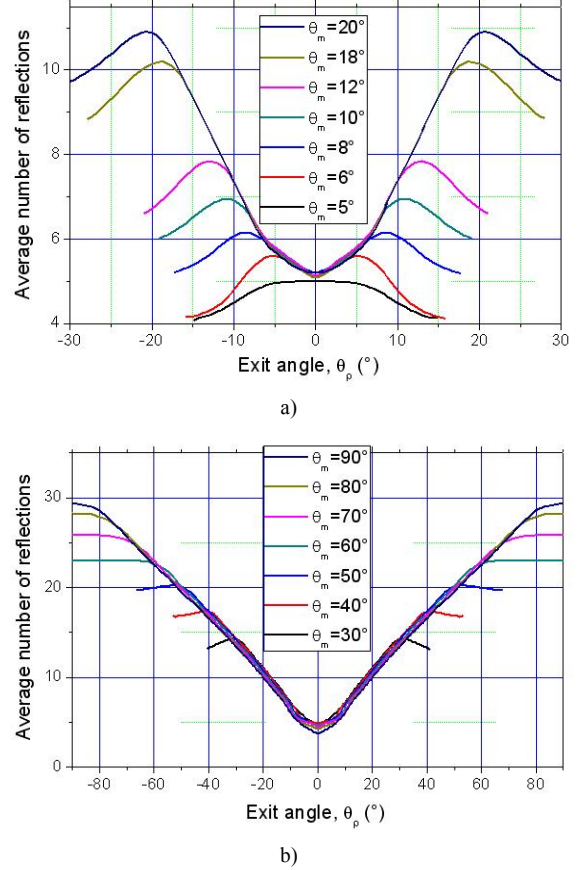


Figure 29. Cartesian representation of the average number of internal reflections of the back reflected rays, as function of exit angle θ_ρ , simulated for $(R'_w, R''_w) = (1.0; 0.9)$. Angular aperture of input beam: (a) $5^\circ, 6^\circ, 8^\circ, 10^\circ, 12^\circ, 18^\circ, 20^\circ$; (b) $30^\circ, 40^\circ, 50^\circ, 60^\circ, 70^\circ, 80^\circ, 90^\circ$

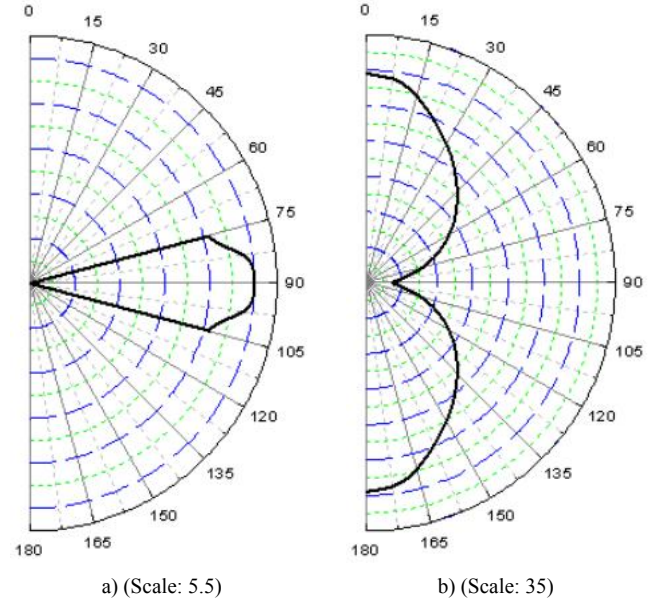


Figure 30. Polar representation of $\bar{N}_\rho(1.0, 0.9, \theta_m, \theta_\rho)$ for $\theta_m = 5^\circ$ (a) and 90° (b)

5. Analysis of the Absorbed Flux

5.1. Optical Absorption Efficiency

From the data of transmission efficiency and reflection efficiency we immediately derive the “absorption efficiency” by the expression [1]:

$$\alpha_{dir}^{lamb}(R_w, \theta_m) = 1 - \tau_{dir}^{lamb}(R_w, \theta_m) - \rho_{dir}^{lamb}(R_w, \theta_m) \quad (33)$$

The absorption efficiency $\alpha_{dir}^{lamb}(R_w, \theta_m)$, calculated for the wall reflectivities $R_w = 0.9$ and 0.8 , is shown in Fig. 31. The simulation with $R_w = 1.0$ is useless in this case, as it would give a systematic zero absorption efficiency. For $\theta_m < \theta_{acc}^{coll} = 5^\circ$, the absorption of light is due to the internal reflections of mainly the transmitted rays, these reflections being about 2, as we see in Fig. 6.

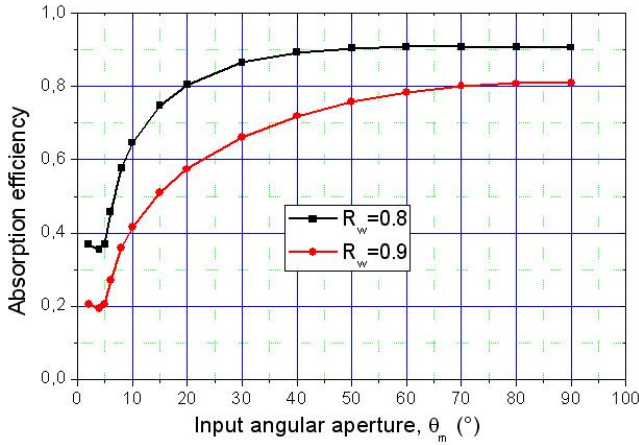


Figure 31. Absorption efficiency $\alpha_{dir}^{lamb}(R_w, \theta_m)$ of the 3D-CPC calculated for two wall reflectivities: $R_w = 0.9$ and 0.8

As a result, the absorption of the incident flux will be $\approx 2 \times 10\%$ when $R_w = 0.9$, and $\approx 2 \times 20\%$ when $R_w = 0.8$, as it can be seen in Fig. 31. For $\theta_m > \theta_{acc}^{coll}$, the absorption of light inside the CPC increases due to the contribution given by the back reflected rays, whose average number of internal

reflections increases from 4 to 16 at increasing θ_m from 4° to 90° (see Fig. 28).

5.2. Distribution of the Absorbed Flux

Here we study how the absorbed flux is distributed inside the CPC. At this purpose a value of wall reflectivity $R_w < 1$ was selected. After each irradiation, by selecting the internal wall of the CPC, the simulation program produces a map of the absorbed flux, projected on the x/y plane orthogonal to the optical axis z . In this way, the map is an annulus with outer radius that of input aperture, $a = 12.035$ mm, and with inner radius that of output aperture, $a' = 1.052$ mm (see Section 2). The intensity map is the projection on the x/y plane of the absorbed irradiation (in W/m^2). Some maps of the absorbed flux are shown in Fig. 32 for the wall reflectivity $R_w = 0.9$, a typical value for realistic solar concentrators.

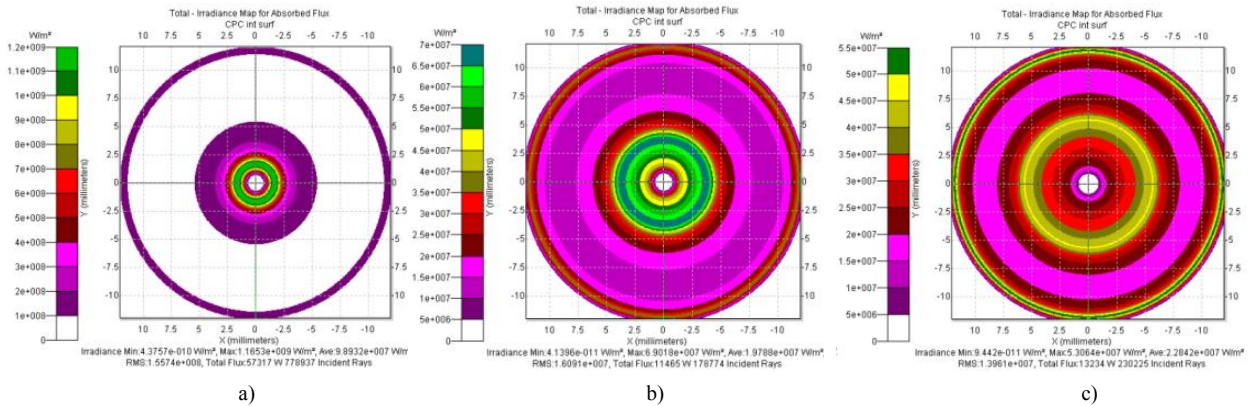
The angular aperture of the lambertian beam has been varied from 10° to 90° . From Fig. 32 we can see that the flux density on the wall progressively moves from the exit to the input aperture, and, starting from 60° , the region adjacent to the exit opening is completely devoid of flux.

It is interesting to study in detail the average distribution of the flux along the z coordinate (the optical axis). To do this, we take the radial profiles of the maps of Fig. 32, plotted as function of the z coordinate, and apply to them the correction factor $\cos \alpha$, to remove the projection operation made by the program, where α is the angle that the tangent to the CPC profile makes with the optical axis, given by [2]:

$$\alpha = \frac{\pi}{2} - \arctg\left(\frac{dz}{dx}\right) = \frac{\pi}{2} + \dots \quad (34)$$

$$\dots - \arctg\left\{\left[\frac{e}{2\sqrt{b^2 - 4(f \cdot x + c)} \cdot \sin \theta_{acc}^{coll}} - d\right] \cdot (16f \cdot \sin \theta_{acc}^{coll})\right\}$$

where x is the coordinate on the axis perpendicular to the optical axis and passing through the center of the exit opening, while z is the coordinate on the optical axis, measured from the center of the exit opening [2].



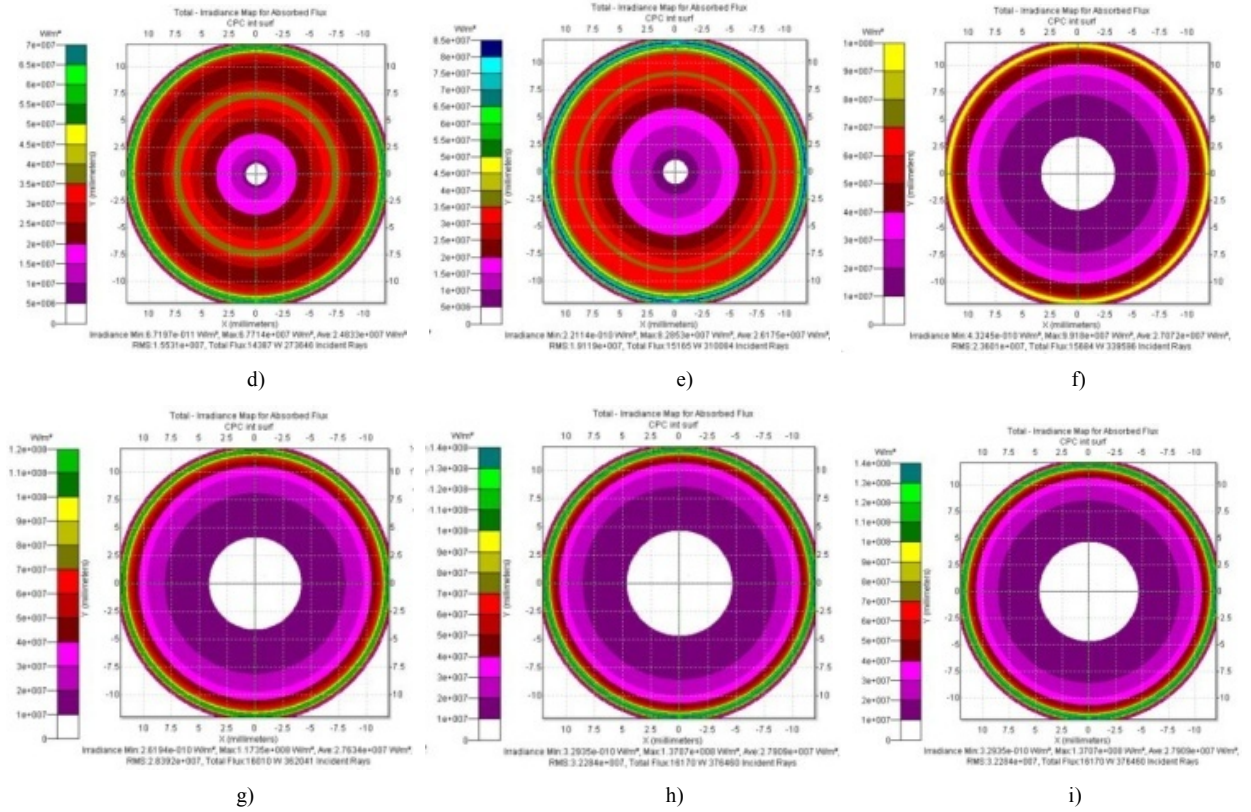


Figure 32. Maps of the flux density on the internal wall, projected on the x/y plane orthogonal to the optical axis z , simulated for different values of the angular aperture of the lambertian beam at input: $\theta_m = 10^\circ$ (a); 20° (b); 30° (c); 40° (d); 50° (e); 60° (f); 70° (g); 80° (h); 90° (i). Wall reflectivity: $R_w = 0.9$

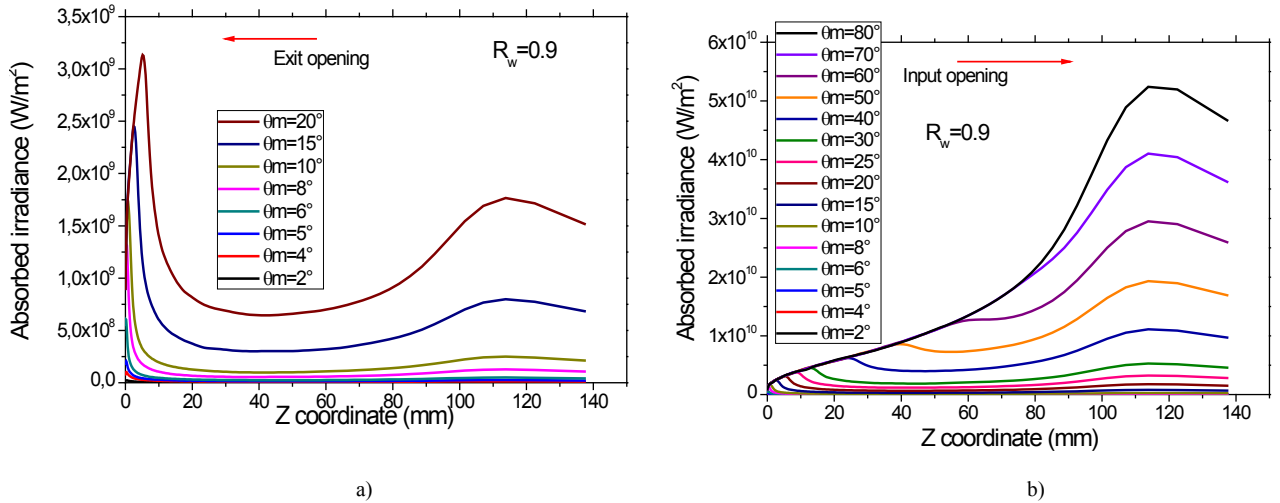


Figure 33. Distribution of the absorption irradiance along the optical axis, from $z = 0$ mm (the exit opening) to $z = 150$ mm (the entrance opening), simulated for angular divergence θ_m from 2° to 20° (a) and from 2° to 80° (b). Wall reflectivity: $R_w = 0.9$

The final result is the profile of the absorbed irradiance, as reported in Fig. 33a for incidence angles in the 0° - 20° interval and in Fig.33b for incidence angles in the 0° - 80° interval. The plot of the irradiance profiles ends at about 137mm, due to the limited resolution of the simulations. The profiles of Fig. 33a show that, at low θ_m values, the flux is restricted in a thin zone near the exit opening, with the peak of irradiance increasing and moving towards higher z

values at increasing θ_m . For $\theta_m \approx 10^\circ$ a large band appears in proximity of the input opening and increases at increasing θ_m , remaining centered at about $z = 115$ mm and leaving a hollow in the center of the CPC. A similar result was observed with parallel beams at input increasing the incidence angle from $\theta_{in} = 0^\circ$ to $\theta_{in} = 20^\circ$ [2]. For θ_m values higher than $\approx 30^\circ$, this band becomes dominant and

most of the flux is absorbed near the input opening (see Fig. 33b). The effect of the increase of the angular divergence of the input beam is ultimately to move much of the flux to the input, as it has been anticipated by the maps of Fig. 32.

6. Conclusions

In conclusion, we have presented the results of optical simulations performed on a 3D-CPC nonimaging concentrator, irradiated in direct mode by a lambertian beam. This simulation work is the second discussing the practical applications of the theoretical methods presented in the first part of the series. The “direct” mode of irradiation is here distinguished by the “inverse” mode of irradiation, which will be discussed in a forthcoming part of the series. In this work we analyze the optical properties of the 3D-CPC with canonical shape (no truncation), with an acceptance angle at collimated light of 5° and maximum exit angle of 90° . The CPC has been analyzed in extreme detail by using a ray-tracing program. We have explored its transmission properties, those of the most practical importance when the 3D-CPC is used in a solar system, in terms of transmission efficiency, spatial and angular distribution of the flux at the output. Generally of less importance is the study of its reflection and absorption properties. Nevertheless, we have dedicated a large part of this paper also to these aspects, applying the same methods used for the transmitted light, because it helps to understand the secret mechanism of light concentration in a CPC.

In the previous work of this series, we have analyzed the optical properties of the CPC irradiated by a collimated beam, oriented at different polar angles respect to the optical axis. In the actual work, we have just modified the geometry of the input beam, using a lambertian beam, that is a beam with cylindrical symmetry and constant radiance. This allowed us to obtain cylindrically symmetric beams at output of the CPC, that have facilitated the elaboration of the results, and to introduce new optical quantities, some already defined in the first theoretical work, others defined for the first time in this work. As in this work we have dealt with the CPC as if it were a generic optical element, we believe it will help to introduce into the routine work of the optical design new methods of simulation to be applied universally to the optical devices.

REFERENCES

- [1] Parretta, A., 2013, Optics of Solar Concentrators. Part 1: Theoretical Models of Light Collection, *Int. Journal of Optics and Applications*, 3(4), 27–39.
- [2] Parretta, A., Antonini, A., 2013, Optics of Solar Concentrators. Part II: Models of light collection of 3D-CPCs under direct and collimated beams, *Int. Journal of Optics and Applications*, 3(5), 72–102.
- [3] Winston, W., 1974, Principles of Solar Concentrators of a Novel Design, *Solar Energy*, 16, 89–95.
- [4] W.T. Welford and R. Winston, *The Optics of Nonimaging Concentrators*, Light and Solar Energy, Academic Press, 1978.
- [5] W.T. Welford and R. Winston, *High Collection Nonimaging Optics*, San Diego, Academic Press, 1989.
- [6] R. Winston, J.C. Miñano, P. Benítez, *Nonimaging Optics*, Elsevier Academic Press, 2005.
- [7] A. Luque, *Solar Cells and Optics for Photovoltaic Concentration*, Adam Hilger, Bristol and Philadelphia, 1989.
- [8] J. Chaves, *Introduction to Nonimaging Optics*, CRC Press, 2008.
- [9] J.J. O’Gallagher, *Nonimaging Optics in Solar Energy*, Morgan & Claypool Publishers, Lexington, KY, 2008.
- [10] Antonini, A., Butturi, M.A., Di Benedetto, P., Uderzo, D., Zurru, P., Milan, E., Stefancich, M., Armani, M., Parretta, A., Baggio, N., 2009, Rondine® PV Concentrators: Field Results and Developments, *Progress in Photovoltaics*, 17, 451–459.
- [11] Parretta, A., Martinelli, G., Bonfiglioli, E., Roncati, D., Antonini, A., Butturi, M.A., Di Benedetto, P., Uderzo, D., Zurru, P., Milan, E., 2009, Indoor Optical Characterization of the Nonimaging “Rondine” PV Solar Concentrator, *Proc., 24th EU PVSEC*, Hamburg, Germany, 747–752.
- [12] Parretta, A., Martinelli, G., Antonini, A., Vincenzi, D., 2010, Direct and inverse methods of characterization of solar concentrators, *Proc., Optics for Solar Energy (SOLAR), Advancing the Science and Technology of Light*, The Westin La Paloma, Tucson, AZ, USA, StuA1.
- [13] Parretta, A., Antonini, A., Butturi, M.A., Di Benedetto, P., Uderzo, D., Zurru, P., 2010, Optical Methods for Indoor Characterization of Small-Size Solar Concentrators Prototypes, *Advances in Science and Technology*, Trans Tech Publications, Switzerland, 74, 196–204.
- [14] Parretta, A., Antonini, A., Stefancich, M., Franceschini, V., Martinelli, G., Armani, M., 2007, Characterization of CPC solar concentrators by a laser method, in *Optical Modeling and Measurements for Solar Energy Systems*, ed. by Daryl R. Myers, *Proc. SPIE Vol. 6652*, pp. 665207 1–12.
- [15] Parretta, A., Zampierolo, L., Roncati, D., 2010, Theoretical aspects of light collection in solar concentrators, *Proc., Optics for Solar Energy (SOLAR), Advancing the Science and Technology of Light*, The Westin La Paloma, Tucson, AZ, USA, StuE1.
- [16] Parretta, A., Morvillo, P., Privato, C., Martinelli, G., Winston, R., 2002, Modelling of 3D-CPCs for concentrating photovoltaic systems, *Proc., PV in Europe, from PV Technology to Energy Solutions*, Rome, Italy, WIP-Munich and ETA-Florence, 547–550.
- [17] A. Antonini, M. Stefancich, J.Coventry, A. Parretta, 2013, Modelling of compound parabolic concentrators for photovoltaic applications, *Int. Journal of Optics and Applications*, 3(4), 40–52.
- [18] Parretta, A., Bonfiglioli, E., Zampierolo, L., Butturi, M.A., Antonini, A., 2014, Optical Characterization of “Rondine®” PV Solar Concentrators, *Int. Journal of Optics and Applications*, 4(1), 1–10.

Applications, 4(4A), 25–52.

[19] <http://lambdaires.com/>

[20] Parretta, A., Sarno, A., Tortora, P., Yakubu, H., Maddalena, P., Zhao, J., Wang, A., 1999, Angle-dependent reflectance measurements on photovoltaic materials and solar cells, *Optics Communications* 172, 139–151.